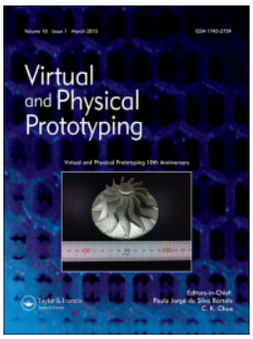

Virtual and Physical Prototyping

ISSN: 1745-2759 (Print) 1745-2767 (Online) Journal homepage: www.tandfonline.com/journals/nvpp20

Reducing solidification cracks and enhancing mechanical performance in additively manufactured Cu-Ti alloys via chemical fluctuation manipulation

Qi Liu , Shengxi Jin , Chuanxi Ren , Dongdong Zhang , Ze Pu , Hongning Wen , Yating Ran , Xingdong Dan , Xuanlai Chen , Song Ni , Jing Lu & Zibin Chen

To cite this article: Qi Liu , Shengxi Jin , Chuanxi Ren , Dongdong Zhang , Ze Pu , Hongning Wen , Yating Ran , Xingdong Dan , Xuanlai Chen , Song Ni , Jing Lu & Zibin Chen (2025) Reducing solidification cracks and enhancing mechanical performance in additively manufactured Cu-Ti alloys via chemical fluctuation manipulation, Virtual and Physical Prototyping, 20:1, e2522274, DOI: 10.1080/17452759.2025.2522274

To link to this article: https://doi.org/10.1080/17452759.2025.2522274

VIRTUAL AND PHYSICAL PROTOTYPING
2025, VOL. 20, NO. 1, e2522274 (21 pages)
https://doi.org/10.1080/17452759.2025.2522274

Taylor & Francis
Taylor & Francis Group

Reducing solidification cracks and enhancing mechanical performance in additively manufactured Cu-Ti alloys via chemical fluctuation manipulation

Qi Liu[a,b], Shengxi Jin[a,b], Chuanxi Ren[a,b], Dongdong Zhang[a,b], Ze Pu[a,b], Hongning Wen[a,b], Yating Ran[a,b], Xingdong Dan[a,b], Xuanlai Chen[a,b], Song Ni[c], Jing Lu[d] and Zibin Chen[a,b]

[a]State Key Laboratory of Ultra-precision Machining Technology, Department of Industrial and Systems Engineering, The Hong Kong Polytechnic University, Hong Kong, People's Republic of China; [b]Research Institute for Advanced Manufacturing, Department of Industrial and Systems Engineering, The Hong Kong Polytechnic University, Hong Kong, People's Republic of China; [c]State Key Laboratory of Powder Metallurgy, Central South University, Changsha, People's Republic of China; [d]Jihua Laboratory, Foshan, People's Republic of China

ABSTRACT

Additive manufacturing offers substantial design freedom for developing copper (Cu) alloy components with complex shapes. However, the extreme process conditions of this technique increase the risk of solidification cracking. Cu-titanium (Ti) alloy, a high-strength Cu alloy, exhibited solidification cracks due to the Ti segregation at grain boundaries when processed with laser powder bed fusion, reducing the appeal of Cu-Ti alloys in the additively manufactured Cu market. In this study, we incorporated chemical fluctuations via in-situ alloying in laser powder bed fusion to suppress solidification cracks. These fluctuations promote the transformation from coarse columnar grains to fine near-equiaxed grains, thereby mitigating solidification cracks at grain boundaries. Furthermore, we discovered that the degree of chemical inhomogeneity decreased with reducing the elemental powder size of in-situ alloying. Utilising this novel strategy, we successfully in-situ synthesised Cu-Ti alloys devoid of solidification cracks and strengthened by cellular microstructures. Compared to Cu-Ti alloys without chemical fluctuations fabricated using pre-alloyed powders, in-situ synthesised Cu-Ti alloys exhibited significantly boosted tensile strength (from 306.3 MPa to 534.7 MPa) and fracture elongation (from 1.8% to 18.4%). This study presents a practical methodology to address the challenge of solidification cracking in some additively manufactured Cu alloys.

ARTICLE HISTORY
Received 12 April 2025
Accepted 15 June 2025

KEYWORDS
Laser powder bed fusion; copper alloy; solidification crack; chemical fluctuation; cellular microstructure

1. Introduction

The industrial sector's demand for complex shapes in copper (Cu) alloy components, such as heat exchangers, electrodes, and windings, has led to the increased use of laser powder bed fusion (L-PBF) for their production [1–3]. This layer-by-layer deposition technique offers substantial design freedom, yet challenges persist in the L-PBF of Cu alloys [4,5]. For instance, solidification cracks were observed in multiple Cu alloy components fabricated through L-PBF, significantly reducing their durability [6–16]. Mao et al. [6] reported the occurrence of solidification cracks in L-PBF-fabricated Cu-Sn alloys despite meticulous optimisation of process parameters. Similarly, Lindström et al. [7] demonstrated that both tin (Sn) and nickel (Ni) promote solidification cracking in Cu alloys, exhibiting dendritic surface morphologies. The formation of solidification cracks in Cu alloys printed by L-PBF is closely related to the segregation of alloying elements. For example, Fang et al. [9] identified chromium (Cr) segregation alongside solidification cracks in L-PBF-produced Cu-Cr-Zr alloys. Furthermore, carbon (C) was found to be segregated along grain boundaries in Cu-C alloys built through L-PBF, triggering solidification cracks [10]. These cracks act as stress concentrators during deformation, leading to premature fracture and severely limiting the mechanical performance of the fabricated components [10,11].

Various methods have been explored to mitigate solidification cracks in Cu alloys. One representative method involves altering the chemical composition of alloys to narrow the solidification temperature range [8,13]. For example, Jadhav et al. [13] demonstrated that decreasing the sulfur (S) content from 910 to 20 ppm in Cu-Sn-S alloys eliminates solidification cracks by preventing

CONTACT Zibin Chen zi-bin.chen@polyu.edu.hk State Key Laboratory of Ultra-precision Machining Technology, Department of Industrial and Systems Engineering, The Hong Kong Polytechnic University, Hong Kong, People's Republic of China; Research Institute for Advanced Manufacturing, Department of Industrial and Systems Engineering, The Hong Kong Polytechnic University, Hong Kong, People's Republic of China

Supplemental data for this article can be accessed online at https://doi.org/10.1080/17452759.2025.2522274.

the formation of low-melting-point liquid films during solidification. However, most elements incorporated in Cu alloys aim to form strengthening phases. Reducing these alloying elements would compromise mechanical properties. Another method focuses on minimising thermal gradients during L-PBF processing to mitigate crack formation [7,17]. Lindström et al. [7] employed a pre-scanning strategy to preheat the substrate, which reduced thermal gradients and successfully suppressed solidification cracks in the lower regions of printed Cu-Ni alloy parts. Nevertheless, crack formation resumed with increasing build height [7], indicating that this method is ineffective in Cu components with complex shapes and taller altitudes. Post-process treatments have also been explored to heal solidification cracks after printing [16,18]. Jóźwik et al. [16] reported that hot isostatic pressing (HIP) effectively eliminated solidification cracks in L-PBF-fabricated Cu-Ni-Si alloys. However, this approach is not cost-effective and will extend production timelines. In brief, previous strategies employed to eliminate solidification cracks in Cu alloys printed by L-PBF present drawbacks. Exploring new approaches to solving solidification cracking is urgently required.

Recently, chemical fluctuations have been proposed as a novel strategy to prevent such cracking in face-centered cubic (FCC) alloys. Ren et al. [19] elucidated that melt convection, controlled by process parameters, diluted the solute concentration at the bottom of the melt pool during L-PBF. The elemental partitioning at the grain boundaries was restricted in these localised solute-deficient regions, which thereby prevented the initiation and propagation of solidification cracks in these areas [19]. However, the risk of cracking in other parts of the melt pool cannot be entirely removed [20,21]. Therefore, chemical fluctuations should be further tailored to affect the grain microstructures of the whole sample, thus stably prohibiting solidification cracks. Moreover, the formation of chemical inhomogeneities in previously studied FCC alloys depended on modulating melt convection. This process is considerably more difficult to control in most Cu alloys due to their low infrared laser absorption and high thermal conductivity. This limitation likely explains why chemical fluctuations have not yet been effectively utilised in Cu alloys to mitigate solidification cracking. Consequently, there is a critical need for an efficient and controllable method to induce chemical fluctuations in L-PBF-processed Cu alloys to suppress solidification cracks. In-situ alloying with elemental powders has been proven effective in generating chemical fluctuations [22,23]. For example, Varoto et al. [22] illustrated that the inhomogeneous distribution of Cr existed in Cu-Cr alloys in situ synthesised with Cu and Cr powders utilising L-PBF. Consequently, employing the in-situ alloying strategy to trigger chemical fluctuations for reducing solidification cracks should be feasible.

Ti serves as an effective alloying element for enhancing the mechanical properties of Cu [24]. However, Cu-Ti alloys processed by L-PBF frequently exhibit solidification cracking, thereby limiting their practical application. In the present study, we proposed to suppress solidification cracking in Cu-Ti alloys by implementing in-situ alloying to trigger chemical fluctuations during L-PBF processing. We found that this approach generates controlled chemical fluctuations that promote constitutional supercooling and facilitate heterogeneous nucleation during solidification. The resultant microstructural transformation from coarse columnar grains to refined near-equiaxed grains effectively eliminates solidification cracking. The degree of chemical fluctuation can be precisely regulated by adjusting the particle size distribution of the elemental powder feedstock in the in-situ alloying process. Furthermore, our findings reveal that optimising the magnitude of these chemical fluctuations enables the simultaneous achievement of two critical objectives: (1) complete prevention of solidification cracking and (2) preservation of beneficial strengthening phases. This dual effect leads to significant improvement in the mechanical performance of L-PBF processed Cu-Ti alloys. The developed methodology presents a strategy for crack mitigation in metal additive manufacturing, offering particular promise for the development of high-strength, ductile Cu-based alloys. The principles established in this study may be extended to other alloy systems susceptible to solidification cracking during L-PBF processing.

2. Experimental

2.1. Material preparation

Figure 1(a) presents pre-alloyed Cu-3 wt% Ti (PA-CuTi) powders with particle sizes ranging from 15 to 53 μm. Figure 1(b) shows the elemental powders utilised to in-situ synthesise Cu-3 wt% Ti alloys. Specimens in-situ alloyed with larger Ti powders (15–53 μm) were designated as IS-CuTi-L, whereas those synthesised utilising smaller Ti powders (5–25 μm) were labelled as IS-CuTi-S. The mixture of elemental powders was conducted using a 3D-shaker (Turbula® T2F, WAB Group). Before each batch mixing, 970 g of Cu powder and 30 g of Ti powder were placed in a plastic bottle, which was then sealed in a vacuum bag to prevent oxidation. The mixing parameters were set at 150 rpm for 120 min. After the mixture, Ti powders were uniformly distributed

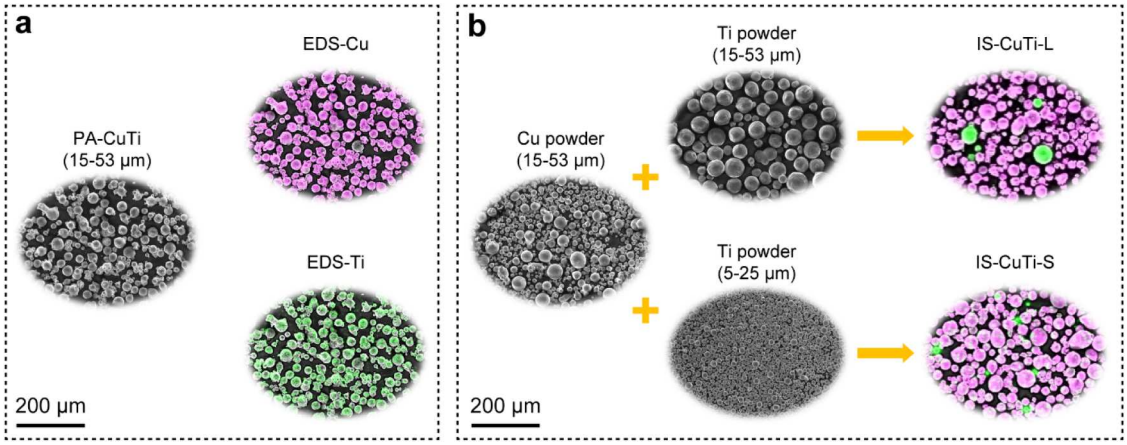

Figure 1. Raw materials for printing Cu-3 wt% Ti alloys. (a) SEM image and EDS maps of pre-alloyed Cu-3 wt% Ti powders; (b) SEM images and EDS maps of elemental powders and the mixed Cu-3 wt% Ti powders.

within the Cu powders, as depicted in Figure 1(b). The laser reflectivity of these mixed powders was measured using a Lambda 950 UV-Vis-NIR spectrophotometer.

Three types of Cu-3 wt% Ti powders were processed using an L-PBF machine (DiMetal-100H), which employed an infrared laser beam with a focused spot size of ~50 μm. To achieve high relative densities in the printed specimens, the volumetric energy density applied to the powder bed was varied by adjusting the laser power to 325, 350, 375, and 400 W, as well as altering the laser scanning speed to 400 and 500 mm/s. All other process parameters were constant across three specimen groups, including a layer thickness of 30 μm, a hatch distance of 60 μm, and a scanning rotation angle of 67° between successive layers. The substrate was 316L stainless steel. Small blocks ($10 \times 10 \times 2.5\ mm^3$) were fabricated to identify the optimal process parameters. Larger blocks ($30 \times 24 \times 2.5\ mm^3$) were printed to characterise the microstructures and evaluate the mechanical properties.

2.2. Microstructure characterisation

For optical microscopy (OM) and scanning electron microscopy (SEM) characterisations, the samples were mechanically polished using a Struers Tegramin-25 auto-polishing machine. Polishing agents, supplied by Struers Co., Ltd., were sequentially used to achieve a mirror-like surface finish, including DiaPro Dac (3 μm diamond), DiaPro Nap (1 μm diamond), and OP-S (0.25 μm fumed silica). For transmission Kikuchi diffraction (TKD) and transmission electron microscopy (TEM) characterisations, thin foils with a thickness of 30 μm were ion milled using a Gatan 695 system. OM images were captured using a ZEISS Axiolab 5 equipped with a ZEISS Axiocam 208 colour microscopy camera. Relative densities of the printed Cu-3 wt% Ti specimens were measured using ImageJ software based on the captured OM images. Secondary electrons (SE), backscattered electrons (BSE), energy dispersive X-ray spectrometry (EDS), electron backscatter diffraction (EBSD), and TKD characterisations were performed via a ThermoFisher Apreo 2S SEM equipped with an Oxford Ultim Max EDS detector and an Oxford Symmetry S3 EBSD detector. Bright-field (BF) and high-resolution (HR) TEM images, as well as scanning transmission electron microscopy (STEM) images, were obtained using a JEOL-2100F operated at 200 kV.

2.3. Mechanical evaluation

The tensile test was conducted at room temperature under a strain rate of $10^{-3}\ s^{-1}$ using a ZwickRoell Z020 TEW universal testing machine equipped with an optical extensometer. The tensile specimens, with gauge dimensions of $10 \times 2 \times 1.5\ mm^3$, were prepared using an electrical discharge machine. Before testing, all specimens were ground with SiC papers up to 2000 grit. The tensile direction was oriented perpendicular to the building direction of the L-PBF process. For each condition, three specimens were tested to ensure the repeatability of the results. Nanoindentation was performed using a FemtoTool NMT04 nanoindenter integrated into a ThermoFisher Apreo 2S SEM. A Berkovich indenter was applied to the specimen surface, achieving a maximum contact depth of 1 μm. Hardness and reduced modulus were measured as functions of contact depth using continuous stiffness measurement [25], which applied a sinusoidal oscillation during loading. The analysis of hardness and reduced modulus was based on data collected at contact depths between 0.7 and 0.8 μm. The relationship

between the reduced modulus (E_r) and the elastic modulus (E) of the tested specimens can be expressed as follows [25]:

$$\frac{1}{E_r} = \frac{1-v^2}{E} + \frac{1-v_i^2}{E_i} \quad (1)$$

where v is the Poisson's ratio of the tested specimen, v_i is the Poisson's ratio of the indenter, and E_i is the elastic modulus of the indenter. Because E_i is much larger than E, and v and v_i are minor, E_r tested by nanoindentation can be utilised to reflect E.

3. Results

3.1. Microstructural characteristic

Figure 2 depicts the formability of the three specimen groups. Cracks are observed in the PA-CuTi specimen under various process parameters. As shown in Figure 2(a), when the volumetric energy density increased from 277.8 to 555.6 J/mm^3, the crack fraction decreased from 1.5% to 0.1%, indicating that high energy density is beneficial to reduce cracks in Cu-Ti alloys printed by L-PBF. However, cracks in the PA-CuTi specimens cannot be eliminated in the present process window. These cracks contribute to the poor relative density of the PA-CuTi specimen, as presented in Figure 2(b). As marked by black arrows in Figure 2(c), cracks oriented parallel to the building direction in L-PBF extend over 100 µm in length. Meanwhile, the high volumetric energy density for restricting cracks induced extensive melt pool disturbance and then pores, which further adversely affected the relative density of the PA-CuTi samples.

In contrast, the IS-CuTi-L and IS-CuTi-S specimens demonstrated broader optimal process windows, achieving relative densities above 99.0% with volumetric energy densities ranging from 400 to 550 J/mm^3 (Figure 2(b)). The defects in the IS-CuTi-L and IS-CuTi-S specimens are dominantly pores, and no cracks were found in these samples, as displayed in Figure 2(d and e). Detailed OM images and defect statistics of the above three specimen groups are exhibited in Supplemental Material S.1. Consequently, a volumetric energy density of 520.8 J/mm^3 was selected to print the three specimen groups, ensuring relative densities exceeding 99.5% and as few cracks as possible, for microstructure characterisation and mechanical

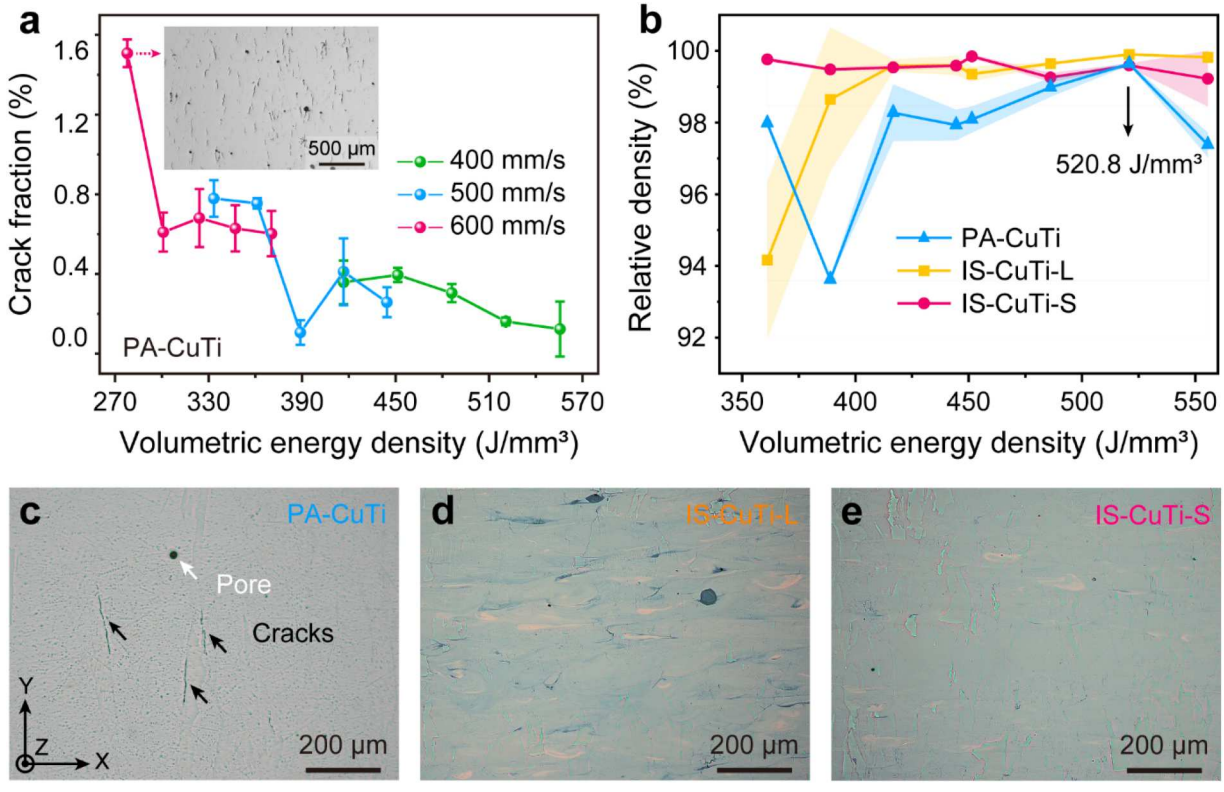

Figure 2. Relative densities and OM images of the printed specimens. (a) Crack fractions plotted as a function of volumetric energy density in the PA-CuTi specimen; (b) relative densities plotted as a function of volumetric energy density across three specimen groups; (c) OM image of the PA-CuTi specimen, (d) OM image of the IS-CuTi-L specimen, (e) OM image of the IS-CuTi-S specimen, each subjected to a volumetric energy density of 520.8 J/mm^3. The X-axis is oriented parallel to the tensile direction, whereas the Y-axis corresponds to the build direction. Subsequent figures maintain this coordinate orientation for consistency.

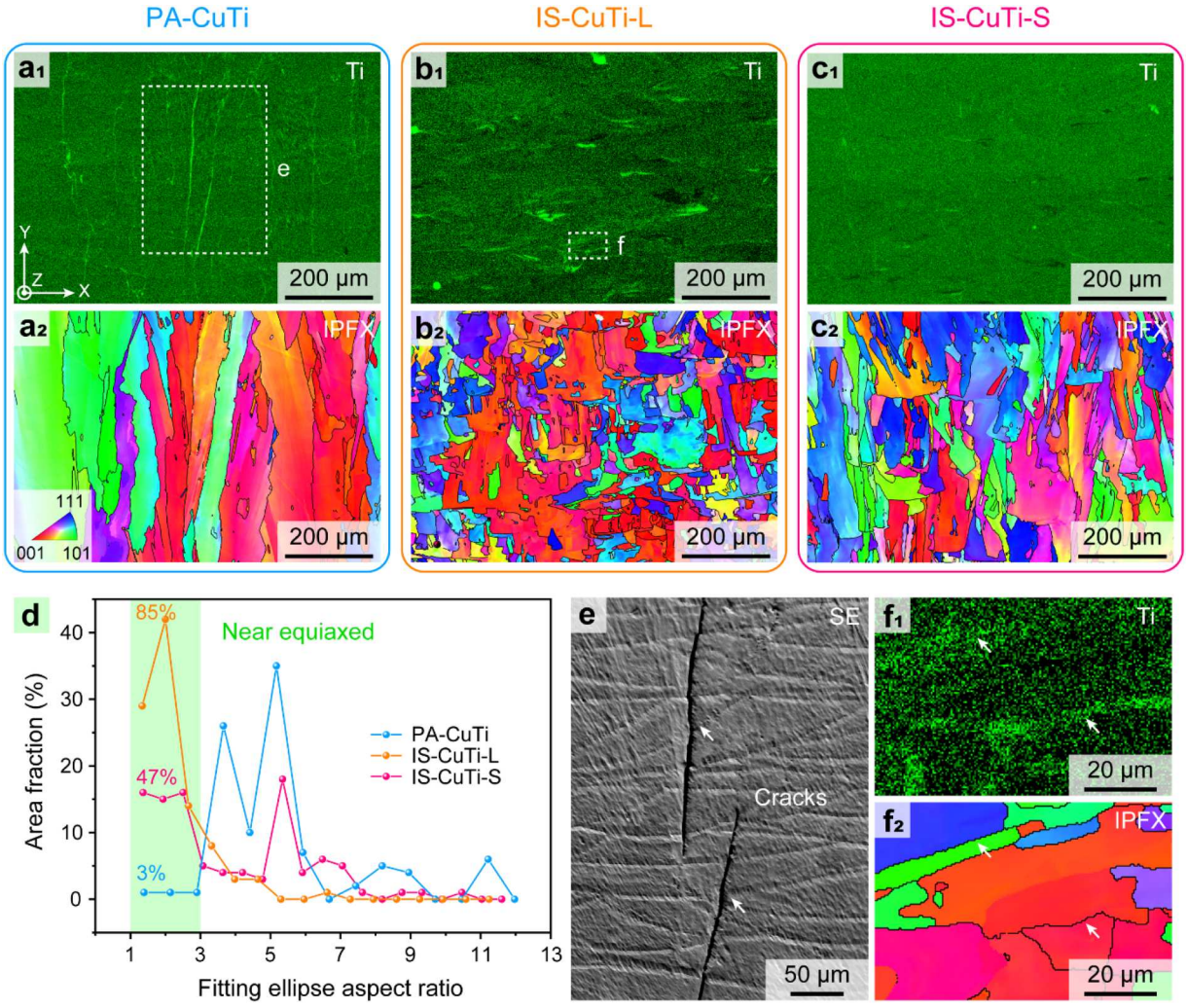

Figure 3. Chemical distributions and grain structures of the printed specimens. EDS maps and grain orientation maps of the (a) PA-CuTi specimen, (b) IS-CuTi-L specimen, and (c) IS-CuTi-S specimen; (d) area fraction of grains categorised by fitting ellipse aspect ratios; (e) SEM image of the region delineated by the white dashed rectangle in (a_1); (f) magnified EDS map and grain orientation map of the region marked by the white dashed rectangle in (b_1).

evaluation. Furthermore, OM images of these specimens exhibit varying colour contrasts. The PA-CuTi specimen displays uniform cyan colouration (Figure 2(c)), while the IS-CuTi-L specimen exhibits yellow and cyan regions with tens of micrometers (Figure 2(d)). The IS-CuTi-S specimen, printed with smaller Ti powders, shows a slight yellow and cyan contrast (Figure 2(e)). These observations suggest the presence of chemical fluctuations in Cu-3 wt% Ti alloys fabricated using elemental powders.

Chemical fluctuations and their impacts on grain structures are illustrated in Figure 3. In the PA-CuTi specimen, the EDS map (Figure 3(a_1)) and the inverse pole figure X (IPFX) colouring map (Figure 3(a_2)) reveal significant Ti segregations at certain grain boundaries, yet no microscale chemical fluctuations are evident. Conversely, the IS-CuTi-L specimen exhibits numerous regions enriched or deficient in Ti (Figure 3(b_1)), indicating substantial chemical fluctuations consistent with observations in Figure 2(c). Moreover, the grain size in the IS-CuTi-L specimen is reduced compared to the PA-CuTi specimen, as depicted in Figure 3(b_2). In-situ alloying utilising smaller Ti powders mitigates chemical fluctuations in the printed specimens, as demonstrated in Figure 3(c_1). Although the grain size of the IS-CuTi-S specimen is slightly larger than that of the IS-CuTi-L specimen, it remains smaller than that of the PA-CuTi specimen (Figure 3(c_2)).

The fitting ellipse aspect ratio was utilised to describe the grain morphology across the three specimen groups, as shown in Figure 3(d). Grains with aspect ratios over 3 are classified as columnar, while those below 3 are near-equiaxed [26]. In the PA-CuTi specimen, near-equiaxed grains constitute only 3% of the observed area, while columnar grains are predominant. In contrast, the area fractions of near-equiaxed grains in the IS-CuTi-L and IS-CuTi-S specimens increase to 85% and 47%,

Table 1. Parameters of grain structures in the printed specimens.

Specimens	PA-CuTi	IS-CuTi-L	IS-CuTi-S
Area fraction of near equiaxed grains (%)	3	85	47
Average grain size (μm)	28.7	16.7	21.9
Density of high-angle grain boundaries (mm^{-1})	34.3	86.6	67.3
Density of low-angle grain boundaries (mm^{-1})	17.7	21.2	14.9

respectively. Table 1 shows other parameters of the grain structures in detail. High-angle grain boundaries exhibit misorientations exceeding 10°, while misorientations of low-angle grain boundaries range from 3° to 10°. Compared to the PA-CuTi specimen, the grain size decreases and the length of the grain boundaries increases in the IS-CuTi-L and IS-CuTi-S specimens.

The region delineated by the white dashed rectangle 'e' in Figure 3(a_1) was further examined under the SE mode, revealing cracks along grain boundaries with significant Ti segregation (Figure 3(e)). The region marked by the white dashed rectangle 'f' in Figure 3(b_1) was observed under high magnification, as shown in Figure 3(f). The Ti-enriched regions (Figure 3(f_1)) impede the growth of columnar grains along the building direction of L-PBF, as illustrated in Figure 3(f_2). These findings indicate that coarse columnar grains transform into fine near-equiaxed grains in Cu-3 wt% Ti alloys due to chemical fluctuations induced by the in-situ alloying strategy with elemental powders.

BSE images and EDS maps were utilised to further examine the influence of chemical fluctuations on cellular microstructures, as illustrated in Figure 4. In the PA-CuTi specimen, cellular microstructures are observed, characterised by cellular walls deficient in Cu but enriched with Ti (Figure 4(a)). The microstructures in the IS-CuTi-L specimen, influenced by chemical fluctuations, were categorised into three distinct types. The first type, indicated by the yellow dot 'A' in Figure 4(b_1), exhibits a low Cu content (Figure 4(b_2)) but a significantly high Ti concentration (Figure 4(b_3)). Quantitative analysis reveals a Ti content of 26.51 wt% at this location (Table 2). This composition corresponds to the eutectoid region of the Cu-Ti phase diagram [24], comprising Cu_4Ti and Cu_3Ti_2 phases. The second type, marked by the yellow dot 'B' in Figure 4(b_1), shows a reduced Ti content of 9.41 wt% compared to the first type (Table 2). Cellular microstructures are evident at this site (Figure 4(c_1)), similar to those observed in the PA-CuTi specimen, with Ti enrichment at the cellular wall and a lower concentration in the interior (Figure 4(c_2)). The third type, denoted by the yellow dot 'C' in Figure 4(b_1), exhibits a relatively low Ti content of 2.53 wt% (Table 2), with no cellular microstructure observed at this location (Figure 4(d)). Consequently, chemical fluctuations altered the solidification behaviour, particularly affecting the formation of cellular microstructures in the printed Cu-3 wt% Ti alloys.

Although chemical fluctuations were also present in the IS-CuTi-S specimen, their magnitude was insufficient to disrupt cellular microstructure formation. In Figure 4(e), cellular microstructures were uniformly distributed, with their assembly directions aligned parallel to the grain growth direction, as indicated by the white lines. The cellular microstructures in the IS-CuTi-S specimen (Figure 4(f_1)) exhibited similar chemical characteristics to those in the PA-CuTi and IS-CuTi-L specimens, with cellular walls deficient in Cu (Figure 4(f_2)) but enriched in Ti (Figure 4(f_3)). Quantitative EDS-point analyses from positions marked by yellow dots in Figure 4(f_1) revealed Ti concentrations of 4.50–5.00 wt % at the cellular walls and less than 3.00 wt% at the interiors (Table 2). Thus, cellular microstructures were successfully achieved in the in-situ synthesised Cu-3 wt% Ti alloys without solidification cracks. Additionally, dark-contrast nanoparticles, identified as Ti oxides, were observed in the BSE images of all three specimens (Supplemental Material S.2).

The phase composition and crystalline orientation of cellular microstructures in the IS-CuTi-S specimen were meticulously elucidated through TEM and TKD analyses, as depicted in Figure 5. The BF-TEM image (Figure 5(a)) reveals that the cellular walls characterised by a high density of dislocations exhibit a pronounced dark contrast, whereas the cellular interiors highlighted in green display rare dislocations. The selected area electron diffraction (SAED) pattern presented in Figure 5(b), acquired at the interface between the cellular wall and interior as shown in Figure 5(a), exclusively reveals diffraction spots corresponding to the $[011]_{Cu}$ zone axis. High-density dislocations within the cellular walls are further corroborated by the dark-field (DF) STEM images (Figure 5(c and d)). TKD characterisations, displayed in Supplemental Material S.3, quantified that the dislocation density within the cellular wall is higher than $2 \times 10^{15}/m^2$. The genesis of these dislocations is ascribed to the tension-compression cycles induced by the recurrent thermal cycles inherent in the L-PBF process [27]. Further examination near an alternative zone axis of the matrix is provided by the BF-TEM image in Figure 5(e), with the corresponding SAED pattern (Figure 5(f)) revealing diffraction spots aligned with the $[001]_{Cu}$ zone axis. Additionally, the HR-TEM image (Figure 5(g)) and its associated fast Fourier transform (FFT) image (Figure 5(h)) unequivocally confirm the exclusive presence of the face-centered cubic (FCC) Cu phase. Prior investigations have demonstrated that diffraction spots of Cu_4Ti precipitates would be discernible under the $[011]_{Cu}$ and $[001]_{Cu}$ zone axes if such

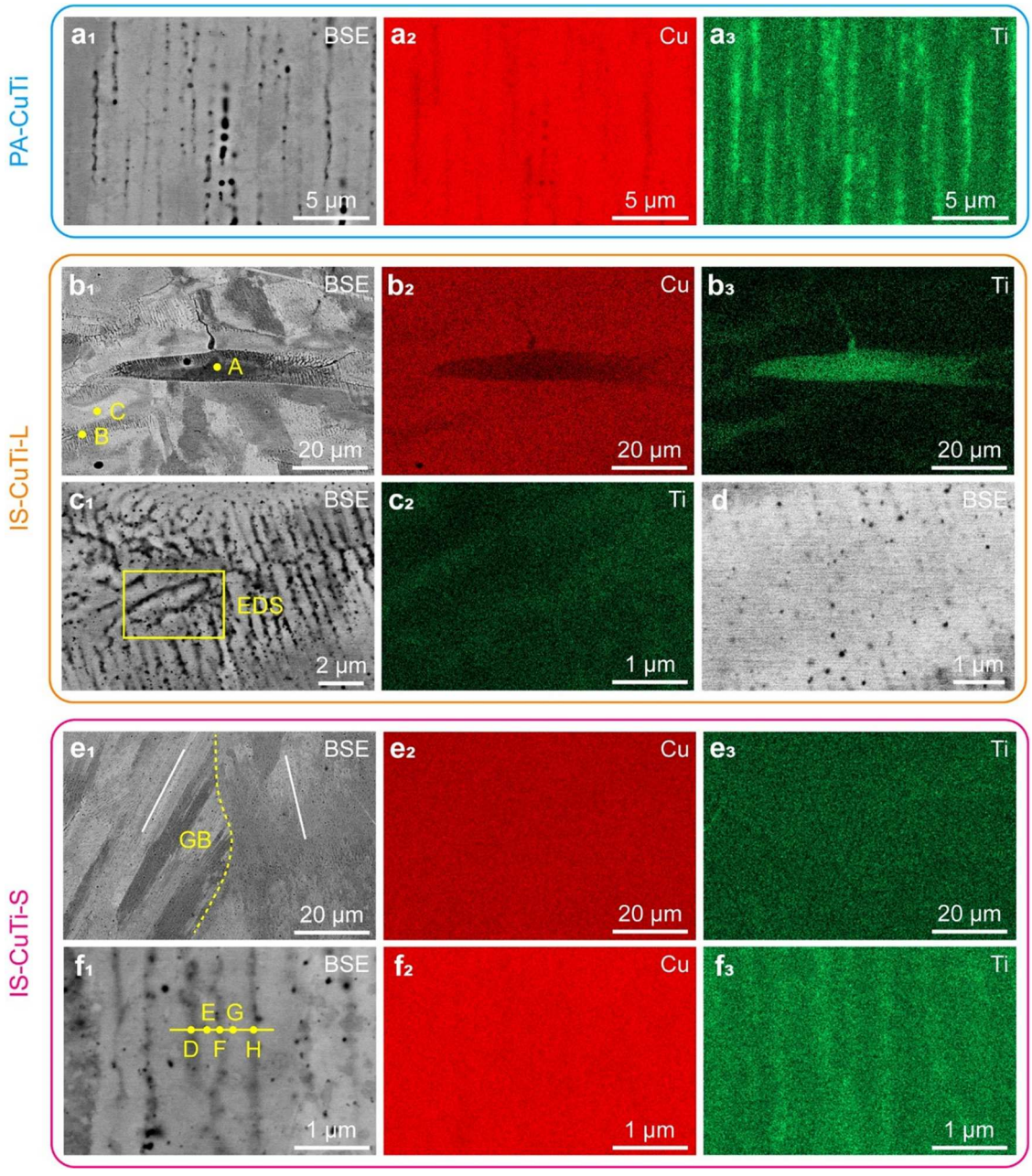

Figure 4. Chemical distributions and cellular microstructures of the printed specimens. BSE images and EDS maps of the (a) PA-CuTi specimen, (b-d) IS-CuTi-L specimen, and (e-f) IS-CuTi-S specimen.

precipitates were present [28,29]. However, in the IS-CuTi-S specimen, only diffraction spots corresponding to the FCC Cu phase were observed, even in regions of the cellular wall enriched with Ti. This suggests that Ti atoms are dissolved with the Cu matrix rather than forming precipitates, a supersaturation phenomenon attributable to the rapid cooling rates characteristic of the L-PBF process [30]. The X-ray diffraction pattern of the IS-CuTi-S specimen (Supplemental Material S.4) also indicated that no Cu_4Ti precipitates existed in the printed Cu-Ti alloys. The region encompassing the cellular microstructures was imaged using a forward-scattered electron detector (FSD), and the corresponding crystalline orientation maps reveal an absence of crystalline misorientations at the interface between the cellular wall and interior (Figure 5(i)).

3.2. Mechanical property

The impact of chemical fluctuations on mechanical performance was evaluated through tensile testing of bulk samples, as depicted in Figure 6. The engineering stress–strain curves and corresponding fracture surface of the three specimen groups are illustrated in Figure 6(a).

Table 2. EDS-point analyses in IS-CuTi-L and IS-CuTi-S specimens.

Num.	A	B	C	D	E	F	G	H
Cu (wt%)	73.49	90.59	97.47	95.23	97.38	95.05	97.29	95.29
Ti (wt%)	26.51	9.41	2.53	4.77	2.62	4.95	2.71	4.71
Error (wt%)	0.97	0.28	0.23	0.42	0.36	0.40	0.37	0.41

The PA-CuTi specimen demonstrates a remarkable enhancement in strength but negligible ductility. Relative to the PA-CuTi specimen, the IS-CuTi-L and IS-CuTi-S specimens exhibit significantly improved strength and ductility. Insets in Figure 6(a) showcase the fracture surfaces of these specimens. The fracture surface of the PA-CuTi specimen reveals cracks that contributed to premature failure. For the fracture surface of the IS-CuTi-L specimen, a microscale cleavage region, encircled by the green dotted line, was observed, suggesting that intense chemical fluctuations induced the fracture. Detailed evidence supporting this observation is provided in Supplemental Material S.5. Conversely, the fracture surface of the IS-CuTi-S specimen only exhibits the dimpled morphology, consistent with its high elongation. For each specimen group, three tensile curves were employed to calculate the average tensile properties, as shown in Supplemental Material S.6. The average tensile properties are presented in Figure 6(b). In particular, the PA-CuTi specimen achieved an ultimate tensile strength (UTS) of 306.3 MPa and a uniform elongation (UE) of 1.6%. In contrast, the IS-CuTi-L specimen attained a UTS of 452.1 MPa and a UE of 10.2%. Further tailoring chemical fluctuations led to an increase in UTS to 534.7 MPa and an enhancement in UE to 12.1% in the IS-CuTi-S specimen. Moreover, the IS-CuTi-S specimen demonstrates superior work-hardening capacity compared to the IS-CuTi-L specimen, as illustrated in Figure 6(c). Compared to other Cu alloys printed by L-PBF, Cu-3Ti alloys fabricated via L-PBF in

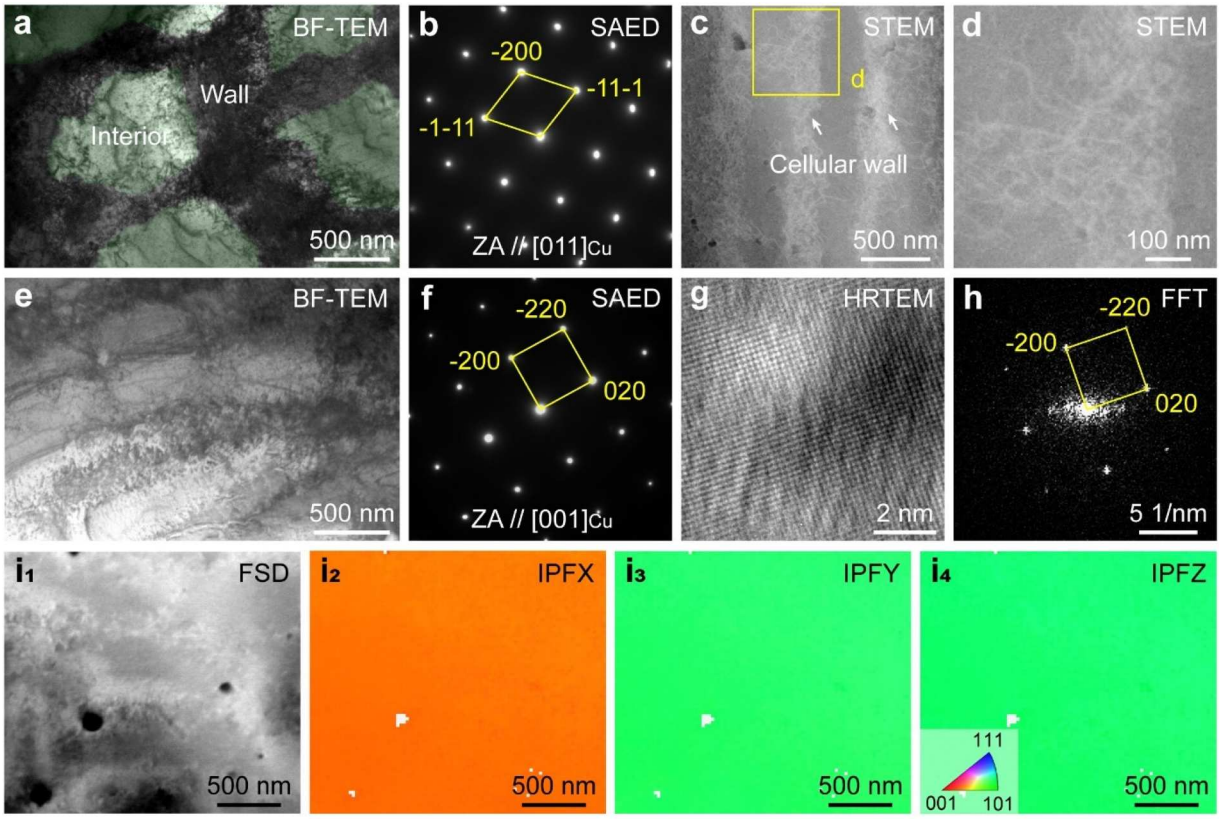

Figure 5. Phase composition and crystalline orientation within the cellular microstructures of the IS-CuTi-S specimen. (a) BF-TEM image illustrating the cellular microstructures, accompanied by (b) the corresponding SAED pattern under the $[011]_{Cu}$ zone axis; (c) DF-STEM image of cellular microstructures; (d) DF-STEM image highlighting the high-density dislocations at the cellular wall; (e) BF-TEM image of cellular microstructures with (f) the corresponding SAED pattern under the $[001]_{Cu}$ zone axis; (g) HR-TEM image and (h) the associated FFT image; (i) TKD images demonstrating a consistent crystalline orientation between the cellular wall and interior.

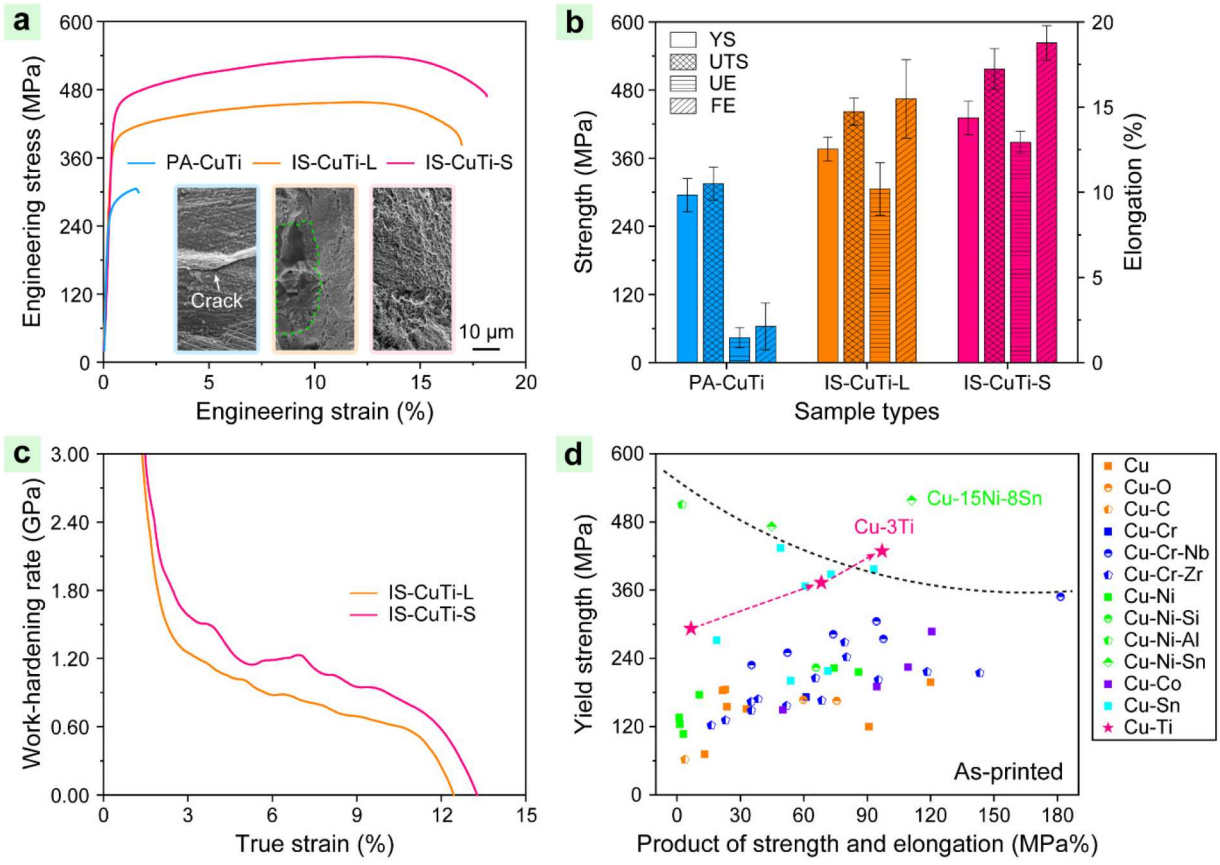

Figure 6. Tensile performance of PA-CuTi, IS-CuTi-L, and IS-CuTi-S specimens. (a) Engineering stress-engineering strain curves and examination of fracture surfaces; (b) comparative analysis of yield strength (YS), UTS, UE, and fracture elongation (FE) of the specimens; (c) work-hardening curves; (d) Ashby map of YS and the product of strength and elongation of Cu-3Ti alloys in this work and other Cu alloys printed by L-PBF [6,10,13,31–57].

this study exhibited a good combination of strength and ductility. After the optimisation of chemical fluctuations, both yield strength and the product of strength and elongation of the printed Cu-Ti alloys are higher than the majority of Cu-Cr and Cu-Ni alloys, as shown in Figure 6(d).

Nanoindentation was performed to elucidate the impact of chemical heterogeneities on localised mechanical properties. In the IS-CuTi-L specimen, distinct microscale hard and soft regions are identified, as depicted in Figure 7(a). The hard regions exhibit a high reduced modulus, whereas the soft regions demonstrate a low reduced modulus (Figure 7(b)). In contrast, the delineation between hard and soft domains in the IS-CuTi-S specimen is less pronounced (Figure 7(c and d)), suggesting a more uniform localised mechanical performance in this sample. The connection between chemical distribution, cellular microstructure, and localised mechanical properties was visually elucidated by characterising the microstructure adjacent to the nanoindentation traces. A region with unevenly distributed Ti was displayed by the EDS-mapping (Figure 7(e)). The corresponding BSE image of this region indicates that the Ti-deficient area lacks cellular microstructures, but the Ti-enriched area exhibits cellular microstructures (Figure 7(f)). The area without cellular microstructures (traces A and B) displays low hardness (less than 2.3 GPa) and modulus (130–160 GPa) values, while the area with cellular microstructures (traces C and D) showcases enhanced hardness (approximately 2.5 GPa) and modulus (140–180 GPa) values (Figure 7(g)). Therefore, chemical fluctuations influence localised mechanical properties by affecting the presence of cellular microstructures.

3.3. Deformation microstructure

In the preceding section, it was elucidated that chemical fluctuations significantly influence both macro and micro mechanical properties. Primarily, these fluctuations were instrumental in mitigating solidification cracking in Cu-Ti alloys, thereby ensuring superior mechanical characteristics. The subsequent inquiry pertains to the observation that IS-CuTi-S specimens, characterised

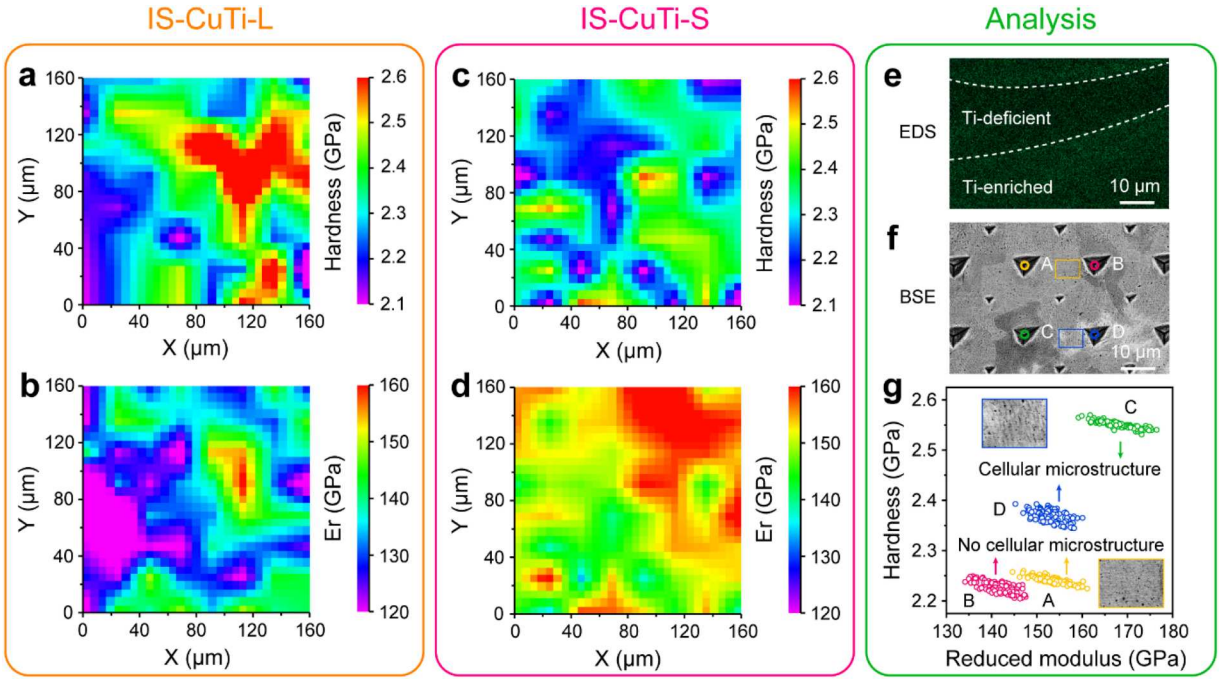

Figure 7. Influence of chemical fluctuations on localised mechanical properties in IS-CuTi-L and IS-CuTi-S specimens. (a) Hardness and (b) reduced modulus maps of the IS-CuTi-L specimen; (c) hardness and (d) reduced modulus maps of the IS-CuTi-S specimen; representative region in the IS-CuTi-L specimen: (e) EDS map of Ti, (f) BSE image, (g) hardness and elastic modulus of the cellular microstructure and no cellular microstructure regions.

by slight chemical fluctuations, exhibit enhanced strength and ductility compared to IS-CuTi-L specimens. Consequently, this section endeavours to elucidate the intrinsic deformation mechanisms responsible for the markedly improved mechanical properties of Cu-Ti alloys through the modulation of chemical fluctuations.

The microstructure features in the deformed Cu-Ti alloys were meticulously examined, as illustrated in Figure 8. Deformation twins and high-density dislocations were observed in the deformed IS-CuTi-L and IS-CuTi-S specimens (Figure 8(a and b)). The geometrically necessary dislocation (GND) density averages 6.2×10^{14} m^{-2} in IS-CuTi-L specimens, increasing to 7.2×10^{14} m^{-2} in IS-CuTi-S specimens (Figure 8(c)). Additionally, numerous low-angle grain boundaries (LAGBs) with misorientations ranging from 3° to 10° were engendered in Cu-Ti alloys during deformation. Quantitative analysis revealed that the LAGBs ratio in Cu-Ti alloys escalates from approximately 20% in their as-printed states to nearly 80% post-deformation (Figure 8(d)). Notably, both the GND density and the LAGBs ratio in the IS-CuTi-L specimen are lower than those in the IS-CuTi-S specimen. Another salient microstructure feature in the deformed Cu-Ti alloys is crystalline rotation. In Figure 8(e), a grain extracted from the IS-CuTi-S specimen exhibits a nearly ⟨111⟩ orientation when observed in the IPFX map. The ⟨111⟩ crystalline orientation is relatively stable in FCC metals when stretched along the observation direction [58]. Hence, variations in crystalline orientation are not readily apparent in the IPFX map. However, the grain undergoes rotation in other directions, leading to variations in crystalline orientations, as depicted in the IPFY and IPFZ maps of Figure 8(e). In summary, the deformed Cu-3 wt% Ti alloys, fabricated via L-PBF using elemental powders, exhibit deformation twins, high-density dislocations, substantially increased LAGBs, and pronounced crystalline rotation.

Intrinsic reasons for the lower GND density and LAGBs ratio in the IS-CuTi-L specimen compared to the IS-CuTi-S specimen post-deformation were investigated in Figure 9. In the deformed IS-CuTi-S specimen, strip-like fluctuations of crystalline orientations are depicted in Figure 9(a_1). Except for the twin boundaries highlighted by the blue lines, numerous LAGBs marked by red lines were observed in the grain interior (Figure 9(a_2)). Additionally, high-density dislocations were homogeneously distributed in the grain interior, as demonstrated in Figure 9(a_3). In contrast, the deformed microstructures in the IS-CuTi-L specimen were uneven. As exhibited in Figure 9(b_1–b_3), the region with obvious strip-like fluctuations of crystalline orientations exhibited abundant LAGBs and dislocations, whereas the region without strip-like fluctuations of crystalline orientations displayed few LAGBs and dislocations. The corresponding EDS map (Figure 9(b_4))

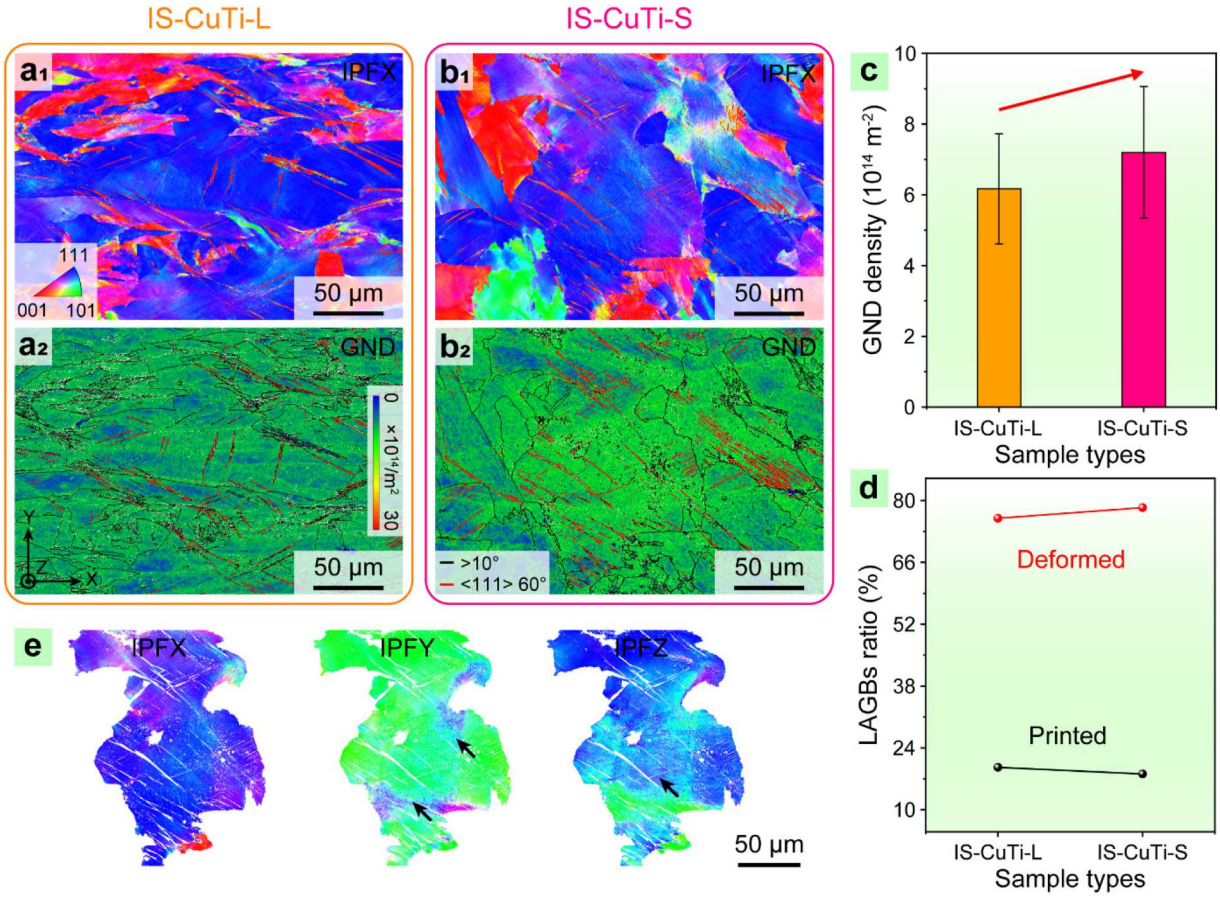

Figure 8. Microstructures of the specimens after tensile deformation. Grain orientation maps of (a_1) IS-CuTi-L, and (b_1) IS-CuTi-S specimens; GND density maps of (a_2) IS-CuTi-L, and (b_2) IS-CuTi-S specimens; (c) average GND density; (d) comparison of the LAGBs ratio in the printed and deformed states; (e) crystalline rotation observed in the IS-CuTi-S specimen.

demonstrated that the region devoid of strip-like fluctuations of crystalline orientations was deficient in Ti. Therefore, the origination of strip-like fluctuations of crystalline orientations was tailored by chemical fluctuations. The enlarged observations in Figures 9(c) and 9(d) further endorsed this declaration. The region with relatively high Ti content (marked by the black rectangle 'c' in Figure 9(b_4)) displayed strip-like fluctuations of crystalline orientations (Figure 9(c_1)). Misorientations (Line-1) between these strip-like fluctuations exceed 3°, defined as LAGBs, as depicted in Figure 9(c_2). Conversely, crystalline orientations in the Ti-deficient region (marked by the black rectangle 'd' in Figure 9(b_4)) were consistent, as exhibited in Figure 9(d_1). Correspondingly, point-to-point misorientations (Line-2) remained below 2° (Figure 9(d_2)). Hence, the Ti-deficient regions induced by intense chemical fluctuations led to the decrement of LAGBs and dislocations in the deformed IS-CuTi-L specimen.

The genesis of strip-like fluctuations of crystalline orientations was illustrated through TKD characterisation, as shown in Figure 10. In Region I, strip-like fluctuations of crystalline orientations were observed in Figure 10(a_1). Coupled with the EDS map of the same area (Figure 10(a_2)), it was found that the cellular wall with high Ti content exhibited one crystalline orientation, while the cellular interior with relatively low Ti content exhibited another crystalline orientation. Misorientations between the cellular wall and the cellular interior were measured over 3° (Figure 10(a_3)). These misorientations were triggered during deformation because no misorientation between the cellular wall and the cellular interior was detected in the printed IS-CuTi-S specimens (Figure 5(i)). The formation of these misorientations is not ascribed to kinking, another strip-like deformation microstructure in metals. The rotation axis of kink bands is parallel to the slip plane and perpendicular to the slip direction [59,60]. For FCC metals with the {111}⟨110⟩ slip system, the rotation axis of the kink band is ⟨112⟩. However, no ⟨112⟩ rotation axis was found between the cellular wall (Point 'A' in Figure 10(a_1)) and the cellular interior (Point 'B' in Figure 10(a_2)) post-deformation, as demonstrated in the {112} pole figure (Figure 10(a_4)).

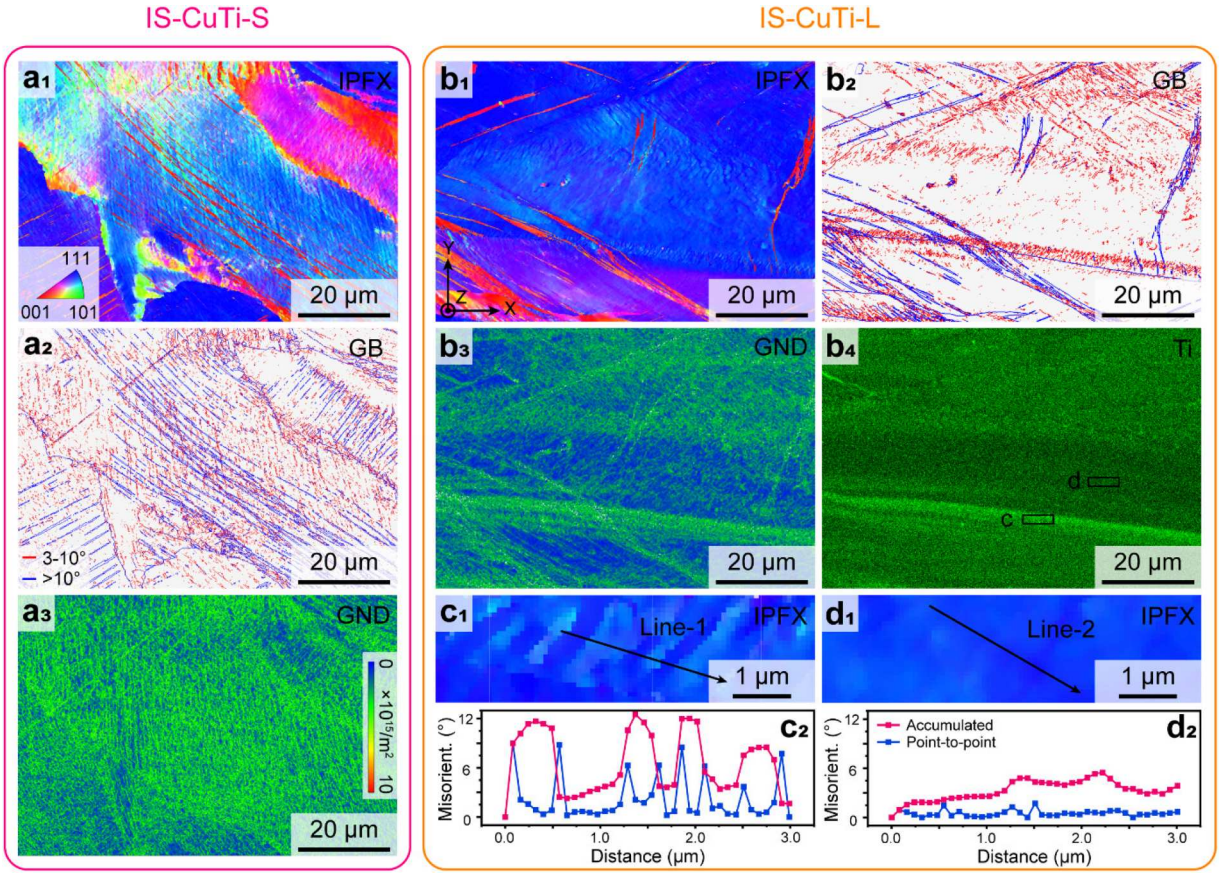

Figure 9. Deformed microstructures influenced by chemical fluctuations in the IS-CuTi-S and IS-CuTi-L specimens. IS-CuTi-S specimen: (a_1) Crystalline orientation map, (a_2) grain boundary map, and (a_3) GND density map; IS-CuTi-L specimen: (b_1) crystalline orientation map, (b_2) grain boundary map, (b_3) GND density map, and (b_4) Ti distribution map; (c_1) crystalline orientation map of the region marked by the black rectangle 'c' in (b_4); (c_2) misorientation along Line-1 in (c_1); (d_1) crystalline orientation map of the region marked by the black rectangle 'd' in (b_4); (d_2) misorientations along Line-2 in (d_1).

Region II of TKD characterisations further confirmed the impact of the crystalline rotation on activating the misorientations between the cellular wall and the cellular interior. In Figure 10(b_1), the region near the grain boundary (marked by the black dashed line) was rotated, while the region away from this grain boundary was not rotated. During deformation, areas adjacent to grain boundaries tended to rotate to preserve the grain boundary integrity, but regions farther from grain boundaries were more stable [61]. Combined with the morphology of cellular microstructures showcased in the FSD image (Figure 10(b_2)), the crystalline orientation tended to be maintained at cellular walls but rotated in cellular interiors. Misorientations along Line-2 only exceeded 3° in the rotated region, as shown in Figure 10(b_3). Consistent with the observations in Region I, no ⟨112⟩ rotation axis was found between the cellular wall (Point 'C' in Figure 10(b_1)) and the cellular interior (Point 'D' in Figure 10(b_1)) in the rotated region (Figure 10(b_4)). Thus, strip-like fluctuations of crystalline orientations are activated by the different crystalline rotations between the cellular wall and cellular interior, which is further manifested as LAGBs observed in Figures 8 and 9.

The influence of cellular microstructures accompanied by their induced crystalline misorientations on dislocation movement was investigated through TEM characterisations, as shown in Figure 11. The cellular microstructures retained their original morphology post-deformation (Figure 11(a)). The SAED pattern was acquired from the interface between the cellular wall and interior in Figure 11(a), where diffraction spots parallel to the $[011]_{Cu}$ zone axis were divided into two sets with a misorientation of approximately 3° (Figure 11(b)). The divided diffraction spots confirmed the crystalline misorientations between the cellular wall and interior formed during deformation. The formation of misorientations enhanced the ability of cellular microstructures to pin dislocations. Consequently, numerous dislocations were confined within the cellular interior, as shown in the BF-TEM image under the $g = 111$ two-beam condition (Figure 11(c)).

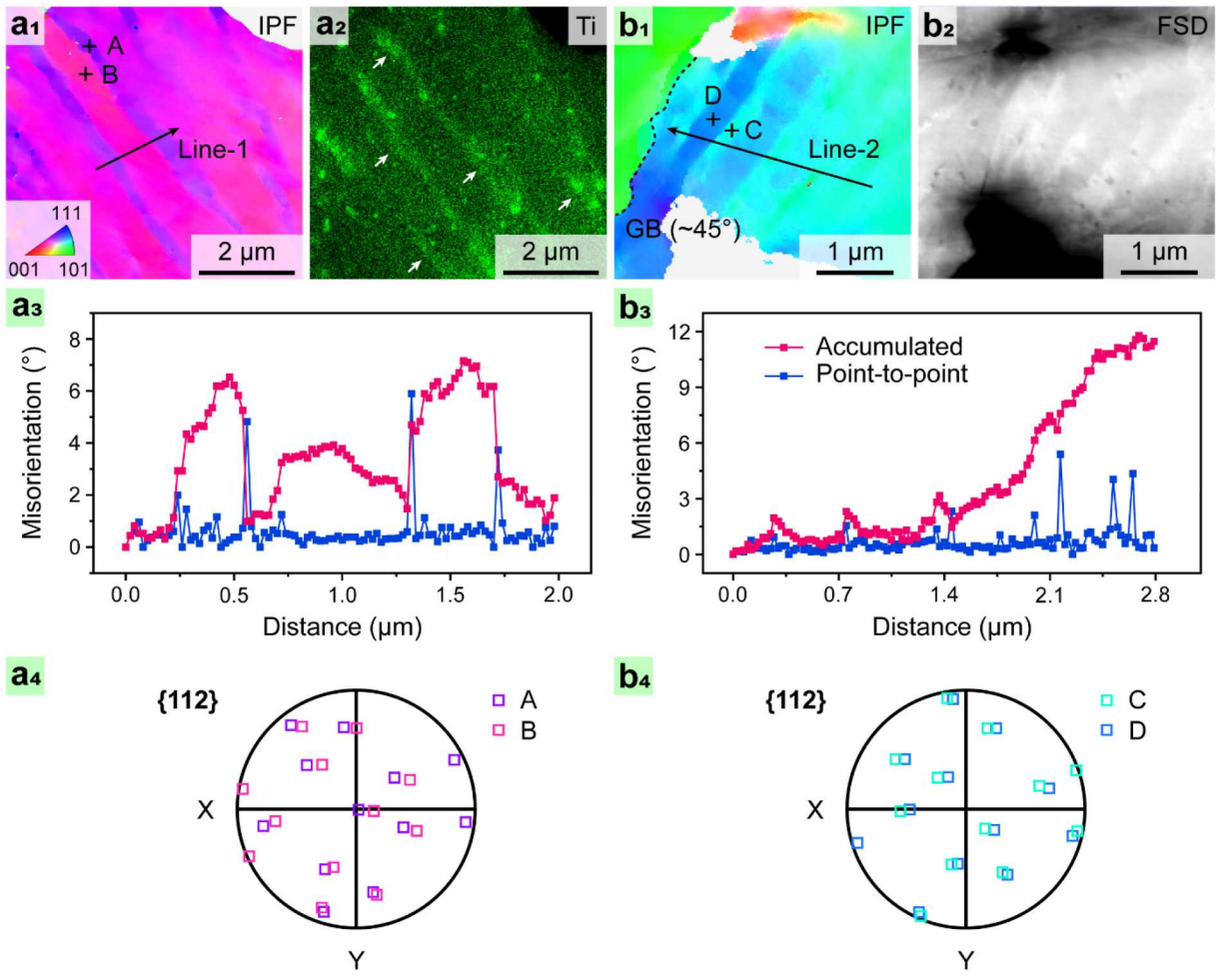

Figure 10. Misorientations between the cellular wall and the cellular interior formed during deformation in the IS-CuTi-S specimen. (a) Region I and (b) Region II of TKD characterisations.

Except for cellular microstructures, deformation twins also inhibited the dislocation movement. BF-TEM image (Figure 11(d)) and the corresponding SAED pattern (Figure 11(e)) identified the deformation twins in the deformed Cu-Ti alloys. Abundant dislocations were accumulated near the boundaries of deformation twins, as indicated by the cyan arrows in Figure 11(f). Therefore, both cellular microstructures and deformation twins contribute positively to the strength of Cu-Ti alloys by effectively hindering dislocation motion.

4. Discussion

4.1. Origination and influence of chemical fluctuation

In this study, chemical fluctuations play a critical role in Cu-3 wt% Ti alloys. Firstly, specimens exhibiting chemical fluctuations were free from cracks and demonstrated an outstanding combination of strength and ductility. Secondly, chemical fluctuations influenced the formation of cellular microstructures, thereby affecting the localised mechanical properties and deformation behaviour. Thirdly, the mechanical performance of Cu-3 wt% Ti alloys was further enhanced by adjusting the degree of chemical fluctuations. Therefore, understanding the formation mechanisms of these chemical fluctuations in Cu-3 wt% Ti alloys printed via L-PBF with elemental powders is of significant interest.

In the PA-CuTi specimen, no chemical fluctuation was detected, which indicates that the formation of chemical fluctuations was not attributed to the L-PBF process in this study. The probability of the number of Ti powders captured by a single melt pool and the laser reflectivity of the mixed powders should be dominant factors impacting the formation of chemical fluctuations. In the mixed powders (Figure 1(b)), though Ti powders were uniformly embedded in Cu powders, the melt pool was insufficient to capture roughly the same number of Ti powders. The discrete probability distribution of elemental powders for in-situ alloying within the bulk specimen prepared by L-PBF, *R*, can be

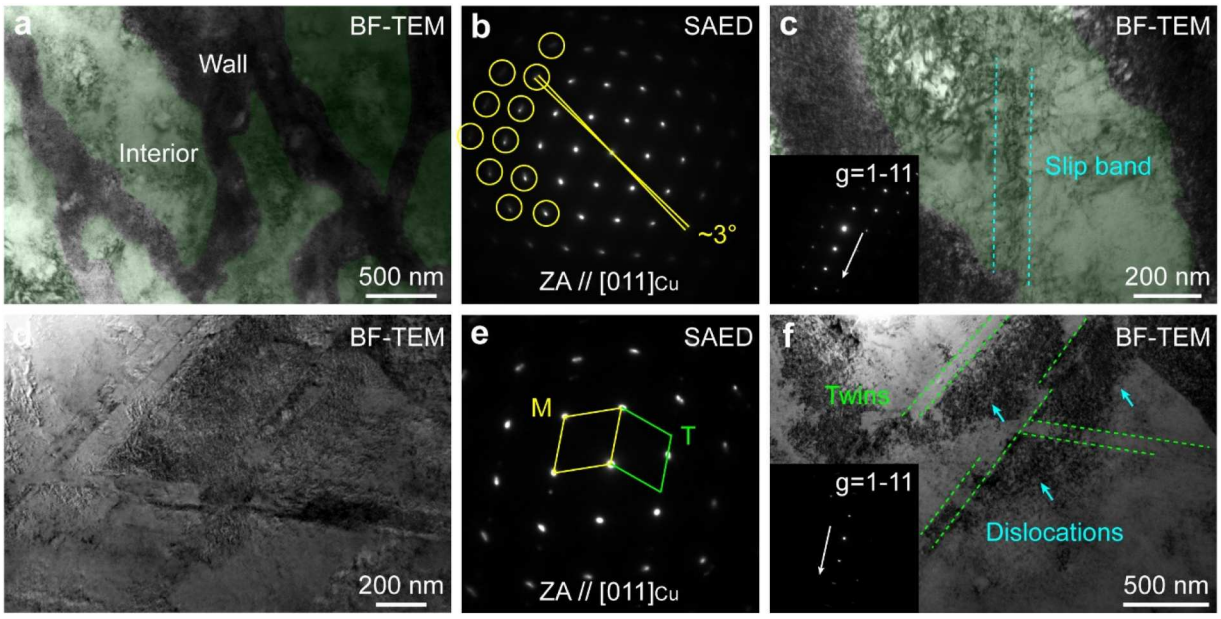

Figure 11. Dislocation movements impacted by cellular microstructures and deformation twins in the IS-CuTi-S specimen. (a) BF-TEM image of cellular microstructures; (b) SAED pattern collected from the interface between the cellular wall and the cellular interior in (a); (c) dislocations at the cellular interior; (d) BF-TEM image of deformation twins; (e) SAED pattern collected from the deformation twins in (d); (f) dislocations restricted by deformation twins.

expressed as follows [62]:

$$R = \frac{(4\lambda)^k e^{-(4\lambda)}}{k!} \tag{2}$$

where k represents the number of alloying powders captured by a single melt pool, and λ is the average rate of powder capture (which is proportional to the square of the melt pool diameter and inversely proportional to the square of the average spacing between alloying powders). This equation also considers the remelting effect between adjacent tracks and layers. The median diameters of large and small Ti powders were measured as 39.5 and 16.0 μm, respectively. The average rate of Ti powders captured by the melt pool was estimated to be 0.73 for large Ti powders and 4.42 for small Ti powders. Consequently, the probability of the number of Ti powders captured by a single melt pool is illustrated in Figure 12(a). The region devoid of Ti powders accounted for approximately 5% in the IS-CuTi-L specimen, which is approaching the experimental value measured in Supplemental Material S.7. Meanwhile, the region containing two Ti powders occupied nearly 25% in the IS-CuTi-L specimen, while the region containing five Ti powders also occupied a high fraction of around 10%. This sharp variation was detrimental to the chemical homogeneity in the as-printed specimens. Therefore, significant chemical fluctuations were observed in the IS-CuTi-L specimen. In contrast, the melt pool in the IS-CuTi-S specimen contained at least 10 small Ti powders (Figure 12(a)), which restricted the formation of Ti-depleted regions. Moreover, due to the reduced Ti powder size, the distinction in the Ti content in different melt pools would decrease, even though they contain slightly different numbers of Ti powders. Hence, reducing the elemental powder size of in situ alloying in L-PBF can effectively decrease the degree of chemical fluctuation. On the other hand, the laser reflectivity of the mixed Cu-3 wt% Ti powders was influenced by the elemental powder size. As exhibited in Figure 12(b), the laser reflectivity of the IS-CuTi-L powders is 79.9% at a wavelength of 1064 nm, which was used in this study. In comparison, the laser reflectivity of the IS-CuTi-S specimen decreased to 68.3%. The reduction of laser reflectivity enhanced the actual energy input on the powder bed during the L-PBF process [63]. The increased energy input further facilitated intense melt flows, which promoted the diffusion of Ti within the melt pool, thereby reducing the chemical fluctuations in the IS-CuTi-S specimen.

The chemical fluctuations affected the grain structures and cellular microstructures in the printed Cu-3 wt% Ti alloys. As observed in Figure 3, chemical fluctuations promoted the transformation from coarse columnar grains to fine near-equiaxed grains. The intrinsic mechanism for grain structure evolution was analyzed as follows. Generally, grain nucleation is controlled by the constitutional supercooling at the solidification front (ΔT_{CS}) and the critical undercooling for nucleation (ΔT_n), if

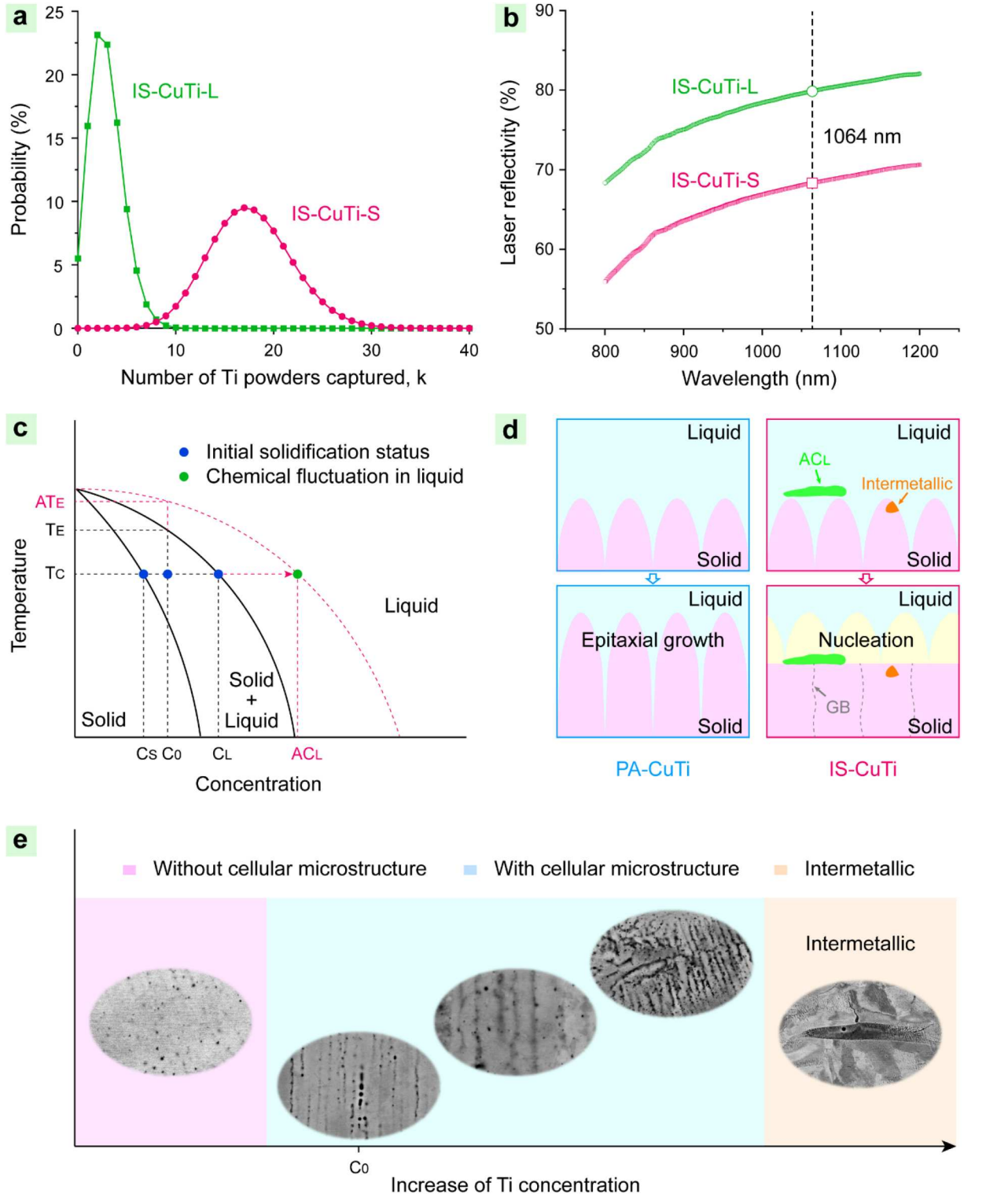

Figure 12. Solidification mechanism of the in situ synthesised Cu-3 wt% Ti alloys via L-PBF. (a) Probability of the number of Ti powders captured by a single melt pool; (b) laser reflectivity curves of IS-CuTi-L and IS-CuTi-S powders; (c) influence of chemical fluctuations in the liquid phase on constitutional supercooling; (d) schematic of grain refinement; (e) schematic of the relationship between Ti concentration and microstructures.

there are no additional nucleation agents [64]. As shown in Figure 12(c), for the alloy with an alloying element concentration, C_0, the constitutional supercooling (ΔT_{cs}) is equal to the liquidus temperature of the alloy (T_E) minus the current temperature of the new liquid after forming a fraction of solid ($T_C s$) [65]. When the

constitutional supercooling (ΔT_{cs}) is larger than the critical undercooling for nucleation (ΔT_n), grain nucleation is triggered [65]. During the solidification process of the in-situ synthesised Cu-3 wt% Ti alloys, the solidification front might approach the Ti-enriched liquid phase. Subsequently, the Ti content in the actual liquid phase was instantaneously increased from the current Ti concentration in the liquid (C_L) to the Ti concentration in the Ti-enriched liquid (AC_L). Assuming the current temperature (T_C) and the current Ti concentration in the solid phase (C_S) did not change instantaneously, the actual liquidus curves should evolve from the black line to the dashed purple line to balance the new solidification system with an increased Ti content in the liquid (AC_L). Therefore, the new constitutional supercooling is equal to the actual liquidus temperature of the solidification system (AT_E) minus the current liquidus temperature (T_C), which is larger than the initial constitutional supercooling ($T_E - T_C$). Consequently, the solidification system exhibits a stronger nucleation tendency when its solidification front approaches the Ti-enriched liquid phase. Except for the improved constitutional supercooling, intermetallics produced by extensive chemical fluctuations, as shown in Figure 4(b), can serve as heterogeneous nucleation sites. A schematic was employed to display the distinction of grain growth between the PA-CuTi and the IS-CuTi specimens (Figure 12(d)). For the PA-CuTi specimen, since no additional nucleation agents appeared in the liquid phase, the nucleation of grains was dominantly controlled by the initial constitutional supercooling ($T_E - T_C$), which was insufficient to restrict the epitaxial growth of grains. Thus, coarse columnar grains formed in the PA-CuTi specimen. In contrast, for the IS-CuTi specimen, both intermetallics and the improved constitutional supercooling ($AT_E - T_C$) promote the nucleation. Therefore, the epitaxial growth of grains was prohibited in the IS-CuTi specimen. Since the chemical fluctuation in the IS-CuTi-S specimen was weaker than that in the IS-CuTi-L specimen, the grain size of the IS-CuTi-S specimen was slightly larger than that of the IS-CuTi-L specimen (Figure 3).

Due to the grain refinement induced by chemical fluctuations, the density of grain boundaries significantly increased (Table 1), which enhanced the total interfacial area to distribute Ti atoms. Therefore, the Ti content at grain boundaries was reduced, inhibiting the tendency of segregation-induced liquation [66]. Moreover, compared to coarse columnar grains, equiaxed grains with abundant LAGBs were beneficial for coordinating the enormous thermal stress formed during the repeated heating/cooling processes of L-PBF [67–71]. Hence, solidification cracks disappeared in the IS-CuTi-L and IS-CuTi-S specimens due to grain refinement via chemical fluctuations. Refining grains to restrict solidification cracks was widely reported as an effective methodology. Unlike previous studies that added nucleation agents or modified process parameters [72–75], this contribution proved that the chemical fluctuations formed during the in-situ alloying in L-PBF were also efficient in realising grain refinement. Significantly, introducing chemical fluctuations to refine grains and further remove solidification cracks is a more general method than finding nucleation agents on a case-by-case basis for different alloys.

Chemical fluctuations also influenced the formation of cellular microstructures, as shown in Figure 12(e). When the localised Ti is extremely high (like 26.5 wt% at Point A in Figure 4(b_1)), the intermetallic phases have a higher nucleation tendency than the Cu-Ti solid solution. Therefore, no cellular microstructures but intermetallics formed in this position. When the localised Ti content decreased (like 9.41 wt% at Point B in Figure 4(b_1)), the liquid phase starts to be solidified as a form of supersaturated solid solution rather than intermetallics. Since the partition of Ti at the liquid phase is higher than that in the solid phase, and thus the concentration of Ti at the liquid phase of interdendritic spaces is higher than that in the dendritic arms. When the temperature further decreased during the solidification, interdendritic spaces solidified as the cellular wall with relatively higher Ti content than the cellular interior. The solidification as a form of cellular microstructures happened in a wide range of localised Ti content. For instance, cellular microstructures were observed in the PA-CuTi and IS-CuTi-S specimens, whose localised Ti contents are approximately 3 wt%. When the localised Ti content decreased to less than 3 wt% in Cu-Ti alloys (like 2.53 wt% at Point C in Figure 4(b_1)), the fraction of the liquid phase in the semi-solid status would decrease, which restricted the formation of cellular microstructures [76]. Therefore, some regions exhibited no cellular microstructure after solidification. In the IS-CuTi-S specimens with weak chemical fluctuations, cellular microstructures were relatively homogeneous, whereas in the IS-CuTi-L specimens with intensive chemical fluctuations, some regions exhibited intermetallic phases or no cellular microstructures.

4.2. Contribution to strength and ductility

With modulating chemical fluctuations, the yield strength of Cu-Ti alloys was gradually increased. Factors contributing to the yield strength of Cu-Ti alloys include grain boundary, oxide, dislocation, solid solution, and cellular microstructure. Contributions of these factors to the yield strength have been estimated based on empirical formulas, as exhibited in Figure 13.

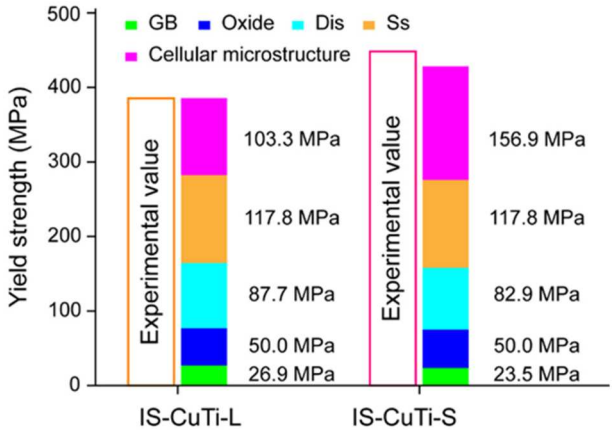

Figure 13. Contributions of grain boundary (GB), oxide, dislocation (Dis), solid solution (Ss), and cellular microstructure to the yield strength in the IS-CuTi-L and the IS-CuTi-S specimens.

The detailed calculations are shown in Supplemental Material S.8. In Figure 13, the contributions of grain boundaries, oxides, dislocations, and solid solutions are similar in the IS-CuTi-L and IS-CuTi-S specimens. The dominant distinction of yield strength originated from the contributions of cellular microstructures. Meanwhile, the calculated values are well-matched with the experimental values in the IS-CuTi-L and IS-CuTi-S specimens.

Although cellular microstructures were successfully introduced into the PA-CuTi specimen, the pre-existing solidification cracks in this sample resulted in brittleness, as shown in Figure 14(a). In other words, the positive influence of cellular microstructures on mechanical properties was shielded by the negative impact of solidification cracks on mechanical properties. In IS-CuTi-L and IS-CuTi-S specimens, solidification cracking was eliminated due to the chemical fluctuations, thereby highlighting the role of cellular microstructures in mechanical performance. As illustrated in Figures 4 and 5, cellular walls in these specimens were enriched with Ti but still retained the FCC structure. It has been reported that cellular microstructures decelerate the dislocation slipping, thus providing high strength and maintaining plasticity [77–79]. Except for the outstanding contribution of cellular microstructures to the yield strength, we found that misorientations induced between the cellular wall and the cellular interior enhanced the ability of cellular microstructures to restrict the dislocation movement during the plastic deformation, further beneficial to the ultimate tensile strength of Cu-Ti alloys (Figure 14(b and c)). Furthermore, deformation twins were observed in the deformed Cu-Ti alloys, which were beneficial to both strength and ductility by facilitating dislocation accumulation.

Compared to the IS-CuTi-L specimen, the IS-CuTi-S specimen exhibited concurrently improved strength and ductility. In the IS-CuTi-L specimen, intense chemical fluctuations triggered intermetallics and regions without cellular microstructures, as exhibited in Figure 14(b_1). Brittle intermetallics with relatively high Ti content led to microcracks during deformation, which is detrimental to the ductility of Cu-Ti alloys (Figure 14(b_2)). Besides, rare dislocations were discovered in the regions without cellular microstructures due to the lack of obstacles to dislocation movement (Figure 14(b_2)), which indicates that these regions sacrifice strength. In contrast, a relatively homogeneous distribution of cellular microstructures in

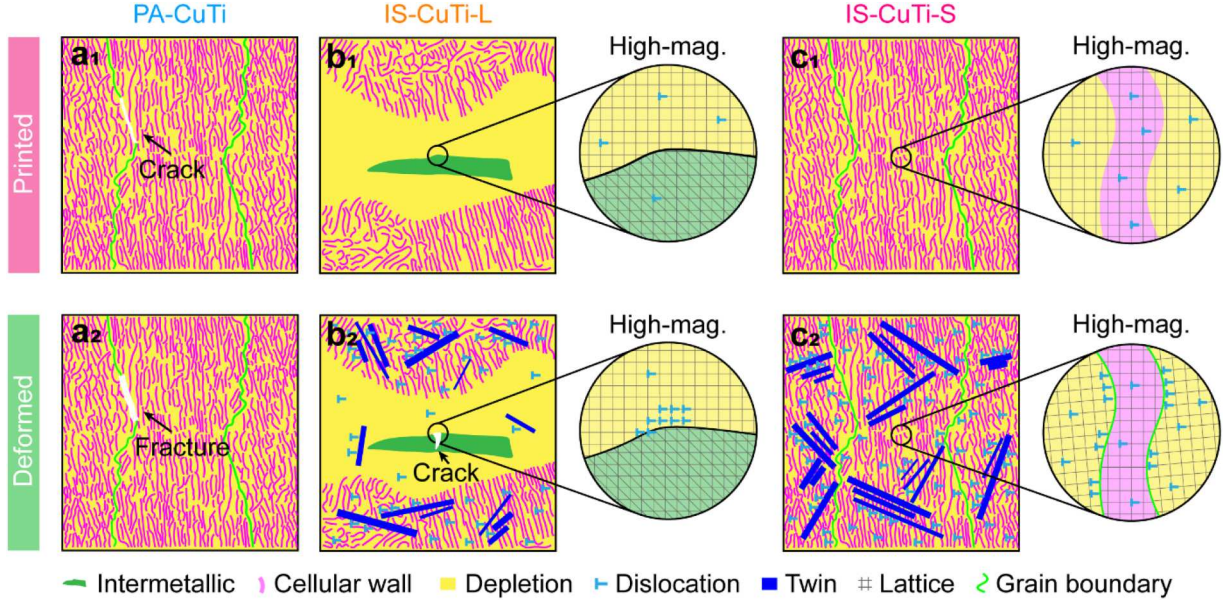

Figure 14. Schematic illustrating the as-printed and deformed microstructures in PA-CuTi, IS-CuTi-L, and IS-CuTi-S specimens.

the IS-CuTi-S specimen enabled a homogeneous distribution of dislocations and twins (Figure 14(c_2)), which thereby resulted in both high strength and ductility.

4.3. Misorientation between the cellular wall and the cellular interior

As demonstrated earlier, the misorientations between the cellular wall and the cellular interior were enhanced during deformation. The underlying mechanism responsible for the formation of these misorientations is discussed in this section. Evidence from Figure 10 shows that these activated misorientations are strongly linked to crystalline rotation. Crystalline rotations are commonly observed in FCC metals during deformation [58,80]. In deformed polycrystals, crystalline rotations are activated to achieve stress equilibrium on either side of the grain boundary [81] and are mediated by dislocation slipping [82]. For instance, Kwon et al. [83] found that in FCC-structured steels, the proportions of ⟨001⟩ and ⟨111⟩ oriented grains increased after tensile deformation, while the proportion of ⟨110⟩ oriented grains decreased. Li et al. [80] investigated grain rotations in Cu via an in-situ tensile test and observed that grain orientation evolved significantly, even during the early stages of tensile deformation. Furthermore, Lebensohn et al. [58] found that intragranular misorientations exceeded 3° in deformed Cu, which was attributed to competition between the ⟨001⟩ and ⟨111⟩ orientations. In their study, this phenomenon was limited to grains with near ⟨111⟩ orientations. In this study, the fluctuations in crystalline orientations were observed in most rotated grains, irrespective of their initial orientation, as shown in Figure 8, where fluctuations of crystalline orientations were evident even in ⟨111⟩-oriented grains aligned with the tensile axis.

Regarding cellular walls, the dissolution of additional Ti atoms into the Cu matrix leads to increased lattice friction stress. For instance, Liu et al. [84] reported that alloying nickel with iron increased its lattice friction stress from less than 8 MPa to around 50 MPa. Additionally, the high-density dislocations interacting with the cellular walls further contributed to lattice distortion, making the cellular walls less favourable for dislocation slipping. Li et al. [85] observed that grain rotation in high-entropy alloys with low lattice distortion was prominent due to enhanced dislocation mobility, whereas grain rotation was minimal in alloys with high lattice distortion. Consequently, cellular walls with high Ti content are resistant to crystalline rotation during deformation, while cellular interiors with fewer Ti atoms allow for more significant crystalline rotation. Thus, during deformation, cellular walls maintained their original crystalline orientations while cellular interiors rotated, leading to the formation of misorientations between the cellular walls and the cellular interiors. Based on this analysis, the cellular microstructures in Cu-3 wt% Ti alloys contributed to the strip-like fluctuations in crystalline orientations.

5. Conclusions

The main conclusions of this study can be drawn as follows:

(1) We have effectively eliminated solidification cracks in Cu-Ti alloys by in-situ alloying via L-PBF. This achievement is attributed to the introduction of chemical fluctuations, which facilitated the transformation of coarse columnar grains (average grain size of 28.7 μm) into fine, near-equiaxed grains (average grain size of 16.7 μm), thereby preventing chemical segregation along the grain boundaries.
(2) The meticulous modification of chemical fluctuations by optimising powder size during in-situ alloying aids in the production of homogeneously distributed cellular microstructures, which significantly enhances the ultimate tensile strength from 306.3 to 534.7 MPa and increases the fracture elongation from 1.8% to 18.4% in Cu-Ti alloys.
(3) The optimal combination of strength and ductility was achieved in crack-free Cu-3 wt% Ti alloys with homogeneously distributed cellular microstructures. In these alloys, misorientations greater than 3° induced between the cellular wall and the cellular interior during deformation were advantageous in restricting dislocation movement.
(4) The formation of misorientations between the cellular wall and the cellular interior is attributed to crystalline rotation during deformation.

Acknowledgments

The authors would like to express their gratitude to Dr. Ruien Hu and Mr. Kenneth K. H. Cheng from the Department of Industrial and Systems Engineering at The Hong Kong Polytechnic University for their assistance in preparing the raw materials. The authors appreciate Mr. Tsz-hin Fan from the State Key Laboratory of Ultra-precision Machining Technology at The Hong Kong Polytechnic University for his assistance with nanoindentation experiments. Additionally, the authors extend their appreciation to Mr. Tab Cheng from The Hong Kong Polytechnic University Research Facility in 3D Printing for his contributions to the preparation of raw materials.

Author contributions

CRediT: **Qi Liu:** Conceptualization, Data curation, Investigation, Methodology, Visualization, Writing – original draft; **Shengxi Jin:** Data curation, Investigation; **Chuanxi Ren:**

Writing – review & editing; **Dongdong Zhang:** Writing – review & editing; **Ze Pu:** Writing – review & editing; **Hongning Wen:** Writing – review & editing; **Yating Ran:** Investigation, Methodology; **Xingdong Dan:** Writing – review & editing; **Xuanlai Chen:** Investigation; **Song Ni:** Writing – review & editing; **Jing Lu:** Writing – review & editing; **Zibin Chen:** Conceptualization, Funding acquisition, Project administration, Supervision, Validation, Writing – review & editing.

Disclosure statement

No potential conflict of interest was reported by the author(s).

Funding

This work was supported by the [Research Committee of The Hong Kong Polytechnic University (PolyU)]; [PolyU Research and Innovation Office] under grant [BBR5, CD9E, and UARQ]; [Shenzhen Municipal Science and Technology Innovation Commission] under grant [SGDX20230821092100002]; and [State Key Laboratory of Ultra-precision Machining Technology in The Hong Kong Polytechnic University].

Data availability statement

The data that support the findings of this study are available from the corresponding author, [Z. Chen], upon reasonable request. Live link of the dataset: https://pan.baidu.com/s/1NWdxtcO98z3Q4PMuyFuOVQ?pwd=5rja.

References

[1] Aghayar Y, Moazzen P, Behboodi B, et al. Laser powder bed fusion of pure copper electrodes. Mater Des 2024;239:112742. doi:10.1016/j.matdes.2024.112742

[2] Ye S, Liu Z, Feng X, et al. Heterostructure and multiple nano-phases achieve superior strength-ductility-conductivity synergy of laser additive manufacturing copper alloy. Virtual Phys Prototyp. 2024;20:e2437467. doi:10.1080/17452759.2024.2437467

[3] Silbernagel C, Gargalis L, Ashcroft I, et al. Electrical resistivity of pure copper processed by medium-powered laser powder bed fusion additive manufacturing for use in electromagnetic applications. Addit Manuf. 2019;29:100831.

[4] Constantin L, Wu Z, Li N, et al. Laser 3D printing of complex copper structures. Addit Manuf. 2020;35:101268.

[5] Sun Z, Tang C, Soh V, et al. Laser powder bed fusion of 316L stainless steel and K220 copper multi-material. Virtual Phys Prototyp. 2024;19:e2356078. doi:10.1080/17452759.2024.2356078

[6] Mao Z, Zhang DZ, Jiang J, et al. Processing optimisation, mechanical properties and microstructural evolution during selective laser melting of Cu-15Sn high-tin bronze. Mater Sci Eng, A. 2018;721:125–134. doi:10.1016/j.msea.2018.02.051

[7] Lindstrom V, Liashenko O, Zweiacker K, et al. Laser powder bed fusion of metal coated copper powders. Materials (Basel). 2020;13:3493. doi:10.3390/ma13163493

[8] Jin Y, Lu B, Tang X. Crack-free copper alloy coating on aluminum alloy fabricated by laser cladding. Coatings. 2023;13:1491. doi:10.3390/coatings13091491

[9] Fang X, Xia W, Wei Q, et al. Preparation of Cu-Cr-Zr alloy by laser powder bed fusion: parameter optimization, microstructure, mechanical and thermal properties for microelectronic applications. Metals (Basel). 2021;11:1410. doi:10.3390/met11091410

[10] Jadhav SD, Dadbakhsh S, Vleugels J, et al. Influence of carbon nanoparticle addition (and impurities) on selective laser melting of pure copper. Materials (Basel). 2019;12:2469. doi:10.3390/ma12152469

[11] Zhang Y, Yin Y. Investigation into the manufacturing process and properties of BrAl10Fe4 Aluminium-bronze parts by selective laser melting. Mater Technol. 2020;35(13–14):821–835. doi:10.1080/10667857.2019.1701254

[12] Wei C, Liu L, Cao H, et al. Cu10Sn to Ti6Al4V bonding mechanisms in laser-based powder bed fusion multiple material additive manufacturing with different build strategies. Addit Manuf. 2022;51:102588.

[13] Jadhav SD, Fu D, Deprez M, et al. Highly conductive and strong CuSn0.3 alloy processed via laser powder bed fusion starting from a tin-coated copper powder. Addit Manuf. 2020;36:101607.

[14] Speidel A, Gargalis L, Ye J, et al. Chemical recovery of spent copper powder in laser powder bed fusion. Addit Manuf. 2022;52:102711.

[15] Min L, Xiaojie S, Peipei L, et al. Forming quality and wettability of surface texture on CuSn10 fabricated by laser powder bed fusion. AIP Adv. 2022;12:125114. doi:10.1063/5.0122076

[16] Jóźwik B, Radoń A, Topolska S, et al. Influence of SLM printing parameters and hot isostatic pressure treatment on the structure and properties of CuNi3Si1 alloy. J Alloys Compd. 2023;947:169531. doi:10.1016/j.jallcom.2023.169531

[17] Singh S, Palani IA, Dehgahi S, et al. Development of Cu-based shape memory alloy through selective laser melting from elemental powder mixture: processing and Characterization. J Alloys Compd. 2023;961:171029. doi:10.1016/j.jallcom.2023.171029

[18] Jadhav SD, Dadbakhsh S, Chen R, et al. Modification of electrical and mechanical properties of selective laser-melted CuCr0.3 alloy using carbon nanoparticles. Adv Eng Mater. 2019;22:1900946. doi:10.1002/adem.201900946

[19] Ren N, Li J, Zhang R, et al. Solute trapping and non-equilibrium microstructure during rapid solidification of additive manufacturing. Nat Commun. 2023;14:7990. doi:10.1038/s41467-023-43563-x

[20] Ghoussoub JN, Tang YT, Dick-Cleland WJB, et al. On the influence of alloy composition on the additive manufacturability of Ni-based superalloys. Metall Mater Trans A. 2022;53(3):962–983. doi:10.1007/s11661-021-06568-z

[21] Harrison NJ, Todd I, Mumtaz K. Reduction of micro-cracking in nickel superalloys processed by Selective Laser Melting: a fundamental alloy design approach. Acta Mater. 2015;94:59–68. doi:10.1016/j.actamat.2015.04.035

[22] Varoto L, Lhuissier P, Roure S, et al. Multi-scale Cu-Cr composites using elemental powder blending in laser powder-bed fusion. Scr Mater. 2024;242:115957. doi:10.1016/j.scriptamat.2023.115957

[23] Huang J, Issariyapat A, Kariya S, et al. On the viability of in-situ alloyed Ti-1Fe as a strong and ductile alternative to Ti-6Al-4V for laser-based powder bed fusion. Addit Manuf. 2025;105:104788.
[24] Soffa WA, Laughlin DE. High-strength age hardening copper-titanium alloys: redivivus. Prog Mater Sci. 2004;49:347–366. doi:10.1016/S0079-6425(03)00029-X
[25] Oliver WC, Pharr GM. An improved technique for determining hardness and elastic modulus using load and displacement sensing indentation experiments. J Mater Res. 1992;7:1564–1583. doi:10.1557/JMR.1992.1564
[26] Nartu M, Welk BA, Mantri SA, et al. Underlying factors determining grain morphologies in high-strength titanium alloys processed by additive manufacturing. Nat Commun. 2023;14:3288. doi:10.1038/s41467-023-38885-9
[27] Li Z, Cui Y, Yan W, et al. Enhanced strengthening and hardening via self-stabilized dislocation network in additively manufactured metals. Mater Today. 2021;50:79–88. doi:10.1016/j.mattod.2021.06.002
[28] Liao Y, Guo C, Zhou C, et al. Stability of the metastable β′-Cu4Ti phase in Cu Ti alloys: role of the Ti content. Mater Charact. 2023;203:113164. doi:10.1016/j.matchar.2023.113164
[29] Huang L, Cui Z, Meng X, et al. Effects of microelements on the microstructure evolution and properties of ultrahigh strength Cu-Ti alloys. Mater Sci Eng, A. 2021;823:141581. doi:10.1016/j.msea.2021.141581
[30] Dong B, Wang Z, Zhu H, et al. Low neutron cross-section FeCrVTiNi based high-entropy alloys: design, additive manufacturing and characterization. Microstructures. 2022;2:2022003.
[31] Qu S, Ding J, Fu J, et al. High-precision laser powder bed fusion processing of pure copper. Addit Manuf. 2021;48:102417.
[32] Huang J, Yan X, Chang C, et al. Pure copper components fabricated by cold spray (CS) and selective laser melting (SLM) technology. Surf Coat Technol. 2020;395:125936. doi:10.1016/j.surfcoat.2020.125936
[33] Jadhav SD, Goossens LR, Kinds Y, et al. Laser-based powder bed fusion additive manufacturing of pure copper. Addit Manuf. 2021;42:101990.
[34] Qu S, Ding J, Fu J, et al. Anisotropic material properties of pure copper with fine-grained microstructure fabricated by laser powder bed fusion process. Addit Manuf. 2022;59:103082.
[35] Liu Y, Zhang J, Tan Q, et al. Additive manufacturing of high strength copper alloy with heterogeneous grain structure through laser powder bed fusion. Acta Mater. 2021;220:117311. doi:10.1016/j.actamat.2021.117311
[36] Zhang S, Zhu H, Zhang L, et al. Microstructure and properties of high strength and high conductivity Cu-Cr alloy components fabricated by high power selective laser melting. Mater Lett. 2019;237:306–309. doi:10.1016/j.matlet.2018.11.118
[37] Yang X, Wang Y, Zhang W, et al. Laser powder bed fusion fabricated Cu-1.8Cr-1.0Nb-2.0Fe alloy with in-situ precipitation strengthening. Mater Sci Eng, A. 2023;878:145222. doi:10.1016/j.msea.2023.145222
[38] Demeneghi G, Barnes B, Gradl P, et al. Size effects on microstructure and mechanical properties of additively manufactured copper-chromium-niobium alloy. Mater Sci Eng, A. 2021;820:141511. doi:10.1016/j.msea.2021.141511
[39] Seltzman AH, Wukitch SJ. Fracture characteristics and heat treatment of laser powder bed fusion additively manufactured GRCop-84 copper. Mater Sci Eng, A. 2021;827:141690. doi:10.1016/j.msea.2021.141690
[40] Wallis C, Buchmayr B. Effect of heat treatments on microstructure and properties of CuCrZr produced by laser-powder bed fusion. Mater Sci Eng, A. 2019;744:215–223. doi:10.1016/j.msea.2018.12.017
[41] Ma Z, Zhang K, Ren Z, et al. Selective laser melting of Cu-Cr-Zr copper alloy: parameter optimization, microstructure and mechanical properties. J Alloys Compd. 2020;828:154350. doi:10.1016/j.jallcom.2020.154350
[42] Wegener T, Koopmann J, Richter J, et al. Cucrzr processed by laser powder bed fusion-process ability and influence of heat treatment on electrical conductivity, microstructure and mechanical properties. Fatigue Fract Eng Mater Struct. 2021;44:2570–2590. doi:10.1111/ffe.13527
[43] Kuai Z, Li Z, Liu B, et al. Selective laser melting of CuCrZr alloy: processing optimisation, microstructure and mechanical properties. J Mater Res Technol. 2022;19:4915–4931. doi:10.1016/j.jmrt.2022.06.158
[44] Salvan C, Briottet L, Baffie T, et al. Cucrzr alloy produced by laser powder bed fusion: microstructure, nanoscale strengthening mechanisms, electrical and mechanical properties. Mater Sci Eng, A. 2021;826:141915. doi:10.1016/j.msea.2021.141915
[45] Hu Z, Du Z, Yang Z, et al. Preparation of Cu-Cr-Zr alloy by selective laser melting: role of scanning parameters on densification, microstructure and mechanical properties. Mater Sci Eng, A. 2022;836:142740. doi:10.1016/j.msea.2022.142740
[46] Bai YC, Zhao CL, Zhang Y, et al. Additively manufactured CuCrZr alloy: microstructure, mechanical properties and machinability. Mat Sci Eng a-Struct. 2021;819:141528. doi:10.1016/j.msea.2021.141528
[47] Zeng CY, Wen H, Bernard BC, et al. Tensile properties of additively manufactured C-18150 copper alloys. Met Mater Int. 2022;28:168–180. doi:10.1007/s12540-021-01052-0
[48] Jadhav SD, Vleugels J, Kruth JP, et al. Mechanical and electrical properties of selective laser-melted parts produced from surface-oxidized copper powder. Mater Des Process Commun. 2019;2:e94.
[49] Wei S, Zhao Y, Li S-H, et al. Laser powder bed fusion of a Cu-Ni-Al alloy using the compositional grading approach. Scr Mater. 2023;231:115441. doi:10.1016/j.scriptamat.2023.115441
[50] Ventura AP, Marvel CJ, Pawlikowski G, et al. The effect of aging on the microstructure of selective laser melted Cu-Ni-Si. Metall Mater Trans A. 2017;48(12):6070–6082. doi:10.1007/s11661-017-4363-8
[51] Murray T, Thomas S, Wu Y, et al. Selective laser melting of nickel aluminium bronze. Addit Manuf. 2020;33:101122.
[52] Zhang G, Chen C, Wang X, et al. Additive manufacturing of fine-structured copper alloy by selective laser melting of pre-alloyed Cu-15Ni-8Sn powder. Int J Adv Manuf Technol. 2018;96:4223–4230. doi:10.1007/s00170-018-1891-3
[53] Wang J, Zhou XL, Li J, et al. Microstructures and properties of SLM-manufactured Cu-15Ni-8Sn alloy. Addit Manuf. 2020;31:100921.
[54] Zhao C, Wang Z, Li D, et al. Selective laser melting of Cu-Ni-Sn: a comprehensive study on the microstructure, mechanical properties, and deformation behavior. Int J Plast. 2021;138:102926. doi:10.1016/j.ijplas.2021.102926

[55] Deng C, Kang J, Feng T, et al. Study on the selective laser melting of CuSn10 powder. Materials (Basel). 2018;11(4):614. doi:10.3390/ma11040614
[56] Ventura AP, Wade CA, Pawlikowski G, et al. Mechanical properties and microstructural characterization of Cu-4.3 pct Sn fabricated by selective laser melting. Metall Mater Trans A. 2016;48(1):178–187. doi:10.1007/s11661-016-3779-x
[57] Scudino S, Unterdörfer C, Prashanth KG, et al. Additive manufacturing of Cu-10Sn bronze. Mater Lett. 2015;156:202–204. doi:10.1016/j.matlet.2015.05.076
[58] Lebensohn RA, Brenner R, Castelnau O, et al. Orientation image-based micromechanical modelling of subgrain texture evolution in polycrystalline copper. Acta Mater. 2008;56:3914–3926. doi:10.1016/j.actamat.2008.04.016
[59] Cook DH, Kumar P, Payne MI, et al. Kink bands promote exceptional fracture resistance in a NbTaTiHf refractory medium-entropy alloy. Science. 2024;384:178–184. doi:10.1126/science.adn2428
[60] Ma T, Miyazawa T, Fujii T. Crystallographic features of deformation-kink bands in coplanar-double-slip-oriented copper single crystals. Mater Charact. 2021;177:111151. doi:10.1016/j.matchar.2021.111151
[61] Chen P, Mao SC, Liu Y, et al. In-situ EBSD study of the active slip systems and lattice rotation behavior of surface grains in aluminum alloy during tensile deformation. Mater Sci Eng, A. 2013;580:114–124. doi:10.1016/j.msea.2013.05.046
[62] Li H, Thomas S, Hutchinson C. Delivering microstructural complexity to additively manufactured metals through controlled mesoscale chemical heterogeneity. Acta Mater. 2022;226:117637. doi:10.1016/j.actamat.2022.117637
[63] Liu Q, Ren C, Song Z, et al. High-strength and high-conductivity additively manufactured Cu-O alloy enabled by cellular microstructure. Addit Manuf. 2024;88:104244.
[64] Zhang D, Qiu D, Gibson MA, et al. Additive manufacturing of ultrafine-grained high-strength titanium alloys. Nature. 2019;576:91–95. doi:10.1038/s41586-019-1783-1
[65] StJohn DH, Prasad A, Easton MA, et al. The contribution of constitutional supercooling to nucleation and grain formation. Metall Mater Trans A. 2015;46:4868–4885. doi:10.1007/s11661-015-2960-y
[66] Wei Q, Xie Y, Teng Q, et al. Crack types, mechanisms, and suppression methods during high-energy beam additive manufacturing of nickel-based superalloys: a review. Chin. J Mech Eng: Addit Manuf Front. 2022;1:100055.
[67] Zhang J, Gao J, Song B, et al. A novel crack-free Ti-modified Al-Cu-Mg alloy designed for selective laser melting. Addit Manuf. 2021;38:101829.
[68] Li G, Brodu E, Soete J, et al. Exploiting the rapid solidification potential of laser powder bed fusion in high strength and crack-free Al-Cu-Mg-Mn-Zr alloys. Addit Manuf. 2021;47:102210.
[69] Wang Z, Wang X, Chen X, et al. Complete columnar-to-equiaxed transition and significant grain refinement in an aluminium alloy by adding Nb particles through laser powder bed fusion. Addit Manuf. 2022;51:102615.
[70] Sun Z, Tan X, Wang C, et al. Reducing hot tearing by grain boundary segregation engineering in additive manufacturing: example of an AlxCoCrFeNi high-entropy alloy. Acta Mater. 2021;204:116505. doi:10.1016/j.actamat.2020.116505
[71] Wu J, Guo Y, Wang F, et al. Laser additively manufactured crack-free aluminum-bearing high entropy alloys: alloy design, synthesis, cracking inhibition and microstructure evolution effects on their tensile properties. Virtual Phys Prototyp. 2023;18:e2250771. doi:10.1080/17452759.2023.2250771
[72] Zhou SY, Su Y, Wang H, et al. Selective laser melting additive manufacturing of 7xxx series Al-Zn-Mg-Cu alloy: cracking elimination by co-incorporation of Si and TiB2. Addit Manuf. 2020;36:101458.
[73] Kontis P, Chauvet E, Peng Z, et al. Atomic-scale grain boundary engineering to overcome hot-cracking in additively-manufactured superalloys. Acta Mater. 2019;177:209–221. doi:10.1016/j.actamat.2019.07.041
[74] Dan X, Ren C, Song Z, et al. Exceptional strength and ductility in heterogeneous multi-gradient TiAl alloys through additive manufacturing. Acta Mater. 2024;281:120395. doi:10.1016/j.actamat.2024.120395
[75] Liu Z, Han Q, Zhang Z, et al. Design of a novel crack-free precipitation-strengthened nickel-based superalloy and composites for laser powder bed fusion. Virtual Phys Prototyp. 2023;18:e2224769. doi:10.1080/17452759.2023.2224769
[76] Hyer H, Zhou L, Mehta A, et al. Composition-dependent solidification cracking of aluminum-silicon alloys during laser powder bed fusion. Acta Mater. 2021;208:116698. doi:10.1016/j.actamat.2021.116698
[77] Liu C, Wang Y, Zhang Y, et al. Deformation mechanisms of additively manufactured TiNbTaZrMo refractory high-entropy alloy: the role of cellular structure. Int J Plast. 2024;173:103884. doi:10.1016/j.ijplas.2024.103884
[78] Liu C, Zhang L-C, Wang K, et al. Improving strength and plasticity via pre-assembled dislocation networks in additively manufactured refractory high entropy alloy. Acta Mater. 2025;283:120526. doi:10.1016/j.actamat.2024.120526
[79] Feng J, Wang B, Zhang Y, et al. High-temperature creep mechanism of Ti-Ta-Nb-Mo-Zr refractory high-entropy alloys prepared by laser powder bed fusion technology. Int J Plast. 2024;181:104080. doi:10.1016/j.ijplas.2024.104080
[80] Li W, Yang J, Zhang Z, et al. High ductility induced by twin-assisted grain rotation and merging in solid-state cold spray additive manufactured Cu. J Mater Sci Technol. 2025;214:11–15. doi:10.1016/j.jmst.2024.06.032
[81] Margulies L, Winther G, Poulsen HF. In situ measurement of grain rotation during deformation of polycrystals. Science. 2001;291:2392–2394. doi:10.1126/science.1057956
[82] Wang L, Teng J, Liu P, et al. Grain rotation mediated by grain boundary dislocations in nanocrystalline platinum. Nat Commun. 2014;5:4402. doi:10.1038/ncomms5402
[83] Kwon EP, Fujieda S, Shinoda K, et al. Texture evolution and fcc/hcp transformation in Fe-Mn-Si-Cr alloys by tensile deformation. Mater Sci Eng, A. 2010;527:6524–6532. doi:10.1016/j.msea.2010.06.041
[84] Liu X, Pei Z, Eisenbach M. Dislocation core structures and Peierls stresses of the high-entropy alloy NiCoFeCrMn and its subsystems. Mater Des. 2019;180:107955. doi:10.1016/j.matdes.2019.107955
[85] Li J, Yamanaka K, Chiba A. Significant lattice-distortion effect on compressive deformation in Mo-added CoCrFeNi-based high-entropy alloys. Mater Sci Eng, A. 2022;830:142295. doi:10.1016/j.msea.2021.142295